Links Between Faulting, Topography, and Sediment Production During Continental Rifting: Insights From Coupled Surface Process, Thermomechanical Modeling

Lorenz Wolf, Ritske S. Huismans, Delphine Rouby, Robert L. Gawthorpe, Sebastian G. Wolf

JGR Solid Earth

RESEARCH ARTICLE
10.1029/2021JB023490

Links Between Faulting, Topography, and Sediment Production During Continental Rifting: Insights From Coupled Surface Process, Thermomechanical Modeling

Lorenz Wolf[1], Ritske S. Huismans[1], Delphine Rouby[2], Robert L. Gawthorpe[1], and Sebastian G. Wolf[1]

[1]Department of Earth Science, Bergen University, Bergen, Norway, [2]Géosciences Environnement Toulouse, UMR5563 CNRS–IRD–Université de Toulouse, Toulouse, France

Key Points:

- Coupled, thermomechanical models show that during continental rifting, the sediment flux reflects the topographic evolution of rifts
- High crustal strength, slow extension, and efficient surface processes promote strain localization and sediment production
- Model results suggest a time-lag of 2–5 Myr between rifting and the peak in sediment flux

Supporting Information:

Supporting Information may be found in the online version of this article.

Correspondence to:

L. Wolf,
lorenz.michel@uib.no

Citation:

Wolf, L., Huismans, R. S., Rouby, D., Gawthorpe, R. L., & Wolf, S. G. (2022). Links between faulting, topography, and sediment production during continental rifting: Insights from coupled surface process, thermomechanical modeling. *Journal of Geophysical Research: Solid Earth*, *127*, e2021JB023490. https://doi.org/10.1029/2021JB023490

Received 25 OCT 2021
Accepted 6 FEB 2022

Abstract Continental rifts form by extension, and their subsequent evolution depends on the tectonic and climatic boundary conditions. We investigate how faulting, topography, and the evolution of the sediment flux during rifting are affected by these boundary conditions, in particular whether it is possible to correlate tectonic activity, topography, and sediment flux on long timescales (40 Myr). We use a thermomechanical model coupled with a landscape evolution model and present a series of 14 models, testing the sensitivity of the models to crustal strength, extension rate, and fluvial erodibility. The degree of strain localization drives the structural evolution of the modeled rifts: slow extension, high crustal strength, and efficient surface processes promote a high degree of strain localization, resulting in fewer active faults with larger offset. Overall, the magnitude of sediment production correlates with the degree of strain localization. In case of unchanged erosional power and similar amount of extension, systems with slower extension produce more sediment owing to a stronger positive feedback between erosion and fault offset. We observe a characteristic sequence of events, reflecting the morpho-tectonic evolution of rifts: the highest rock uplift rates are observed before the maximum elevation, and the highest sediment flux postdates the peak in elevation. Our results indicate that for natural systems, the evolution of the sediment flux is a good proxy for the evolution of topography, and that a time lag of 2–5 Myr between the peaks in main tectonic activity and sediment flux can exist.

Plain Language Summary Continental rifting is the response of the uppermost part of the Earth to extensional, tectonic forces. The resulting landscape consists of subsided, sediment-filled basins and uplifted, high-elevation rift shoulders. Resolving what contributes to rifting on long-timescales (i.e., tens of millions of years) from natural examples is challenging, since inverting the sedimentary record to resolve correlations between tectonic activity, topography, and the sediment production relies on several assumptions. We use computer models to simulate continental rifting, and subject the models to different boundary conditions. This allows us to have a holistic view of the rifting process under variable conditions over a 40-million-year period, and we assess how the topography, tectonic deformation, and sediment production evolve over time. We see that the degree of localization of deformation is decisive for the evolution of the rifts, and that localization correlates with sediment production. Furthermore, the temporal evolution of the sediment production reflects the tectonic and topographic evolution. Moving from models to natural examples, our findings indicate that the evolution of the sediment production is a good proxy for topography. However, a time lag of 2–5 million years could exist between the main tectonic activity and the highest sediment production.

1. Introduction

The Earth's surface is shaped both by tectonic and surface processes. Identifying possible couplings and feedbacks between tectonic and surface processes has been a focus of research during the past decades (e.g., Champagnac et al., 2012; Molnar & England, 1990; Whipple, 2009; Whittaker, 2012). A plethora of studies focused on mountain belts and showed that orographic precipitation can focus deformation and exhumation (Beaumont et al., 1992; Willett, 1999), that spatial and temporal variations in uplift and exhumation can be controlled by erosion (e.g., Enkelmann et al., 2009; Grujic et al., 2006), that variations in erosion reflect variations in tectonically controlled rock uplift (e.g., Adams et al., 2015; Michel et al., 2018; Wang et al., 2014), and how sensitive the orogen-deformation is to erosion and deposition (Erdős et al., 2015; Wolf et al., 2021). In extensional settings, a high lithospheric strength increases rift asymmetry and rift shoulder elevation (e.g., Beucher & Huismans, 2020;

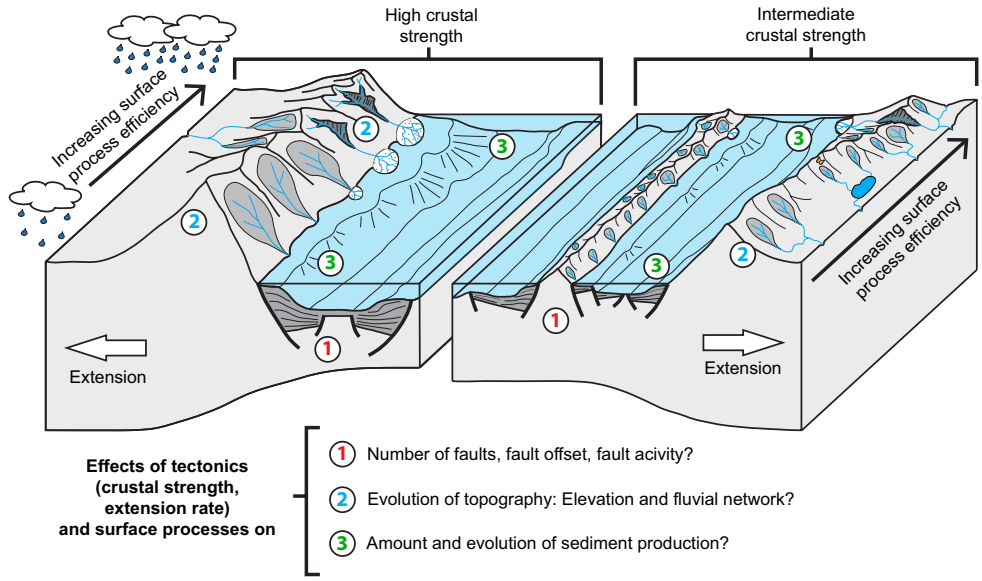

Figure 1. Cartoon illustrating the effects of tectonic and surface processes on the development of rifts. Tectonically-driven extension leads to uplift and subsidence of the landscape, resulting in rift shoulder uplift and basin subsidence. Depending on the crustal strength (left or right part of the cartoon), the resulting rift geometries can be different. Surface processes such as fluvial erosion or hillslope processes lower the elevated landscape and generate sediment. The efficiency of the surface processes affects the topography and the deposition of sediments in the basins (erosion increases from the front toward the back of the cartoon). The numbers indicate specific questions that are addressed in this work, and that are related to the effects of the tectonic (extension rate, crustal strength) and climatic boundary conditions (efficiency of surface processes).

Corti et al., 2018; Theunissen & Huismans, 2019). Studies documented that a feedback between footwall erosion and hanging wall deposition prolongs fault activity and offset (Maniatis et al., 2009; Olive et al., 2014), which enhances the formation of large offset asymmetric normal faults (Beucher & Huismans, 2020; Theunissen & Huismans, 2019), and that enhanced sediment supply to the rift basin owing to an antecedent river network can localize fault displacement (Hemelsdaël et al., 2017). All these studies demonstrate, how sensitive the evolution of orogens and rifts is to both tectonic and climatic boundary conditions.

In continental rifts, tectonically driven faulting leads to uplift and subsidence of the landscape, forming rift basins with high-elevation rift shoulders (Figure 1). Climatically influenced surface processes erode the landscape, create relief, and produce sediments that infill the tectonically generated depressions creating the stratigraphic record of a basin (Figure 1). Variations in the associated sediment flux can be related both to tectonic and climatic causes (e.g., Forzoni et al., 2014; McNeill et al., 2019; Rohais & Rouby, 2020; Sømme et al., 2019) and in turn, the preserved stratigraphic record is often used to unravel the effects of tectonic or surface processes, for instance, by inferring the history of rock uplift, the evolution of topography and the drainage network, and climatic variations (e.g., Armitage et al., 2011; Castelltort & Van Den Driessche, 2003; Geurts et al., 2020; Guillocheau et al., 2012; Rohais & Rouby, 2020; Stevens Goddard et al., 2020; Sømme et al., 2019; Whittaker et al., 2010). Correlations between catchment area, runoff, relief, and sediment flux observed in present-day river systems (Syvitski & Milliman, 2007) are commonly used to invert the evolution of the sediment flux (as preserved in the stratigraphic record), for instance, for the evolution of past relief and catchment area (e.g., Rohais & Rouby, 2020; Sømme et al., 2019). One of the inherent assumptions for this approach is that temporal variations in the sediment flux are coeval and correlated with changes in relief or catchment area also on long timescales a (e.g., as induced by tectonically controlled changes in rock uplift). However, obtaining independent constraints on past topographic evolution and linking this to sediment flux is challenging.

The simple correlation between tectonic activity, topography, and sediment flux on geologic timescales implicit in the BQART method (relating erodibility [B], water discharge [Q], area [A], relief [R], and temperature [T]) is, furthermore, hampered by the transient response of landscapes to changes in tectonic and/or climatic conditions, and by possible feedbacks between tectonic and surface processes (e.g., Allen, 2008; Allen & Heller, 2011; Li et al., 2018; Whittaker et al., 2010). Here, we aim to circumvent these limitations and obtain coeval constraints on

topography, tectonic activity, and sediment production using coupled forward modeling. We analyze the evolution of continental rifts from the syn-rift to the post-rift using a high-resolution 2D thermomechanical model coupled with a landscape evolution model, and subject the rifts to different tectonic and surface process boundary conditions. The landscape evolution model includes the temporally and spatially transient uplift field of faults and simulates the erosional response of the evolving landscape. In turn, the tectonic model includes the effects of erosion and deposition on the evolution of lithosphere deformation and fault formation. Hence, the model allows investigating the response of tectonics (i.e., evolution of the structure of a rift, number of faults, fault offset) to the redistribution of mass by erosion and sedimentation, and at the same time allows measuring the amount of sediment generated over time. We address the following questions (Figure 1): (a) What is the influence of different key parameters, specifically crustal strength, erosional power, and extension rate on the structural and topographic evolution of rifts? (b) How do the key parameters affect sediment production? (c) How are the evolution of sediment flux, topography, and tectonic activity correlated on long, 10^6–10^7 years, timescales?

The response of sediment production to variations in tectonic and climatic boundary conditions has been the subject of previous work using surface process models (e.g., Armitage et al., 2011; Densmore et al., 2007; Forzoni et al., 2014; Li et al., 2018; Yuan et al., 2019). These models used either simple 1D geometries or were restricted to a limited-spatial extent (i.e., focusing on a single catchment), considered only short timescales (<15 Myr), or simplified the tectonics using uniform uplift fields. Inherent to all of these studies is that they are not able to include the effect of erosion and deposition on fault offset owing to their missing mechanical model. On the other hand, previous work using coupled models in rift settings often used simple tectonic boundary conditions and focused, for instance, solely on the role of the crustal rheology using fixed extension rates (e.g., Andrés-Martínez et al., 2019; Beucher & Huismans, 2020; Olive et al., 2014; Theunissen & Huismans, 2019). These studies demonstrated that rheology affects the coupling between crust and mantle (Beucher & Huismans, 2020; Huismans & Beaumont, 2002, 2003; Theunissen & Huismans, 2019) and showed a feedback between erosion, hanging wall deposition, and fault offset (Andrés-Martínez et al., 2019; Olive et al., 2014; Theunissen & Huismans, 2019). Other work using purely thermomechanical models also highlighted the effect of extension rate on the width, asymmetry, and distribution of deformation of rifts and rifted margins (Brune et al., 2014; Huismans & Beaumont, 2002, 2003; Naliboff et al., 2017; Svartman Dias et al., 2015; Tetreault & Buiter, 2018). We build upon these conclusions and as tectonic boundary conditions, we test the sensitivity of the models to both variable crustal rheologies and different extension rates. In order to test the sensitivity of the models to surface processes, we vary the erodibility between the models.

We present a series of 14 numerical experiments, where we systematically vary the tectonic and surface process efficiency parameters. We focus on elucidating changes in the sediment production both during the syn-rift and post-rift phase and on what the underlying mechanisms are. We analyze the structural and topographic evolution of the rifts and how this impacts the evolution of the sediment flux. For selected models, we provide detailed analyses of fault activity, fault offset, and topography. Furthermore, we relate the temporal evolution of the sediment flux with the temporal evolution of elevation and rock uplift, identifying four phases that reflect the morpho-tectonic evolution of rifts. We finally assess, how our model results corroborate the approach to invert the sediment record for the topographic evolution of rifts.

2. Modeling Methods

2.1. The T-Model: A Coupled Thermomechanical Surface Process Model

We use a lithosphere-scale thermomechanical surface process model to investigate continental rifting (Wolf et al., 2021; see Figure 2a). The model consists of the 2D thermo-mechanical code Fantom (Thieulot, 2011), coupled to the 2D landscape evolution code FastScape (Braun & Willett, 2013; Yuan et al., 2019). FastScape and Fantom are tightly coupled in a T-manner (Beaumont et al., 1992; Wolf et al., 2021), so that uplift and subsidence arising from the thermomechanical model provide a cylindrical uplift signal to FastScape and average erosion and deposition feed back to the thermomechanical computation. The coupled model captures the temporally and spatially transient evolution of continental rifts subject to the interaction between surface processes and tectonics. In the following, we describe the setup and boundary conditions of the tectonic and surface process model and explain the strategy behind our modeling approach.

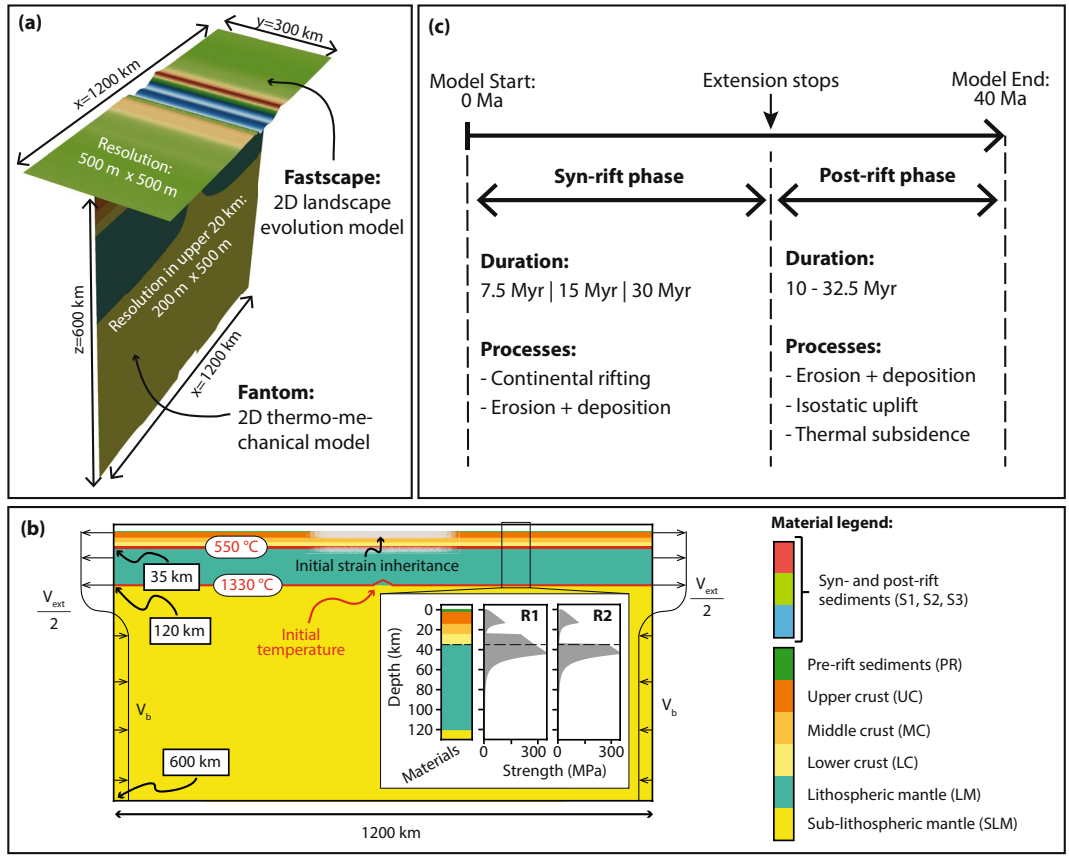

Figure 2. Model setup (a) Overview, model dimensions, and resolutions of the T-model, where a 2D landscape evolution model (FastScape) is coupled with a 2D thermomechanical model (Fantom). (b) Model setup and geometry for Fantom, illustrating the layered structure (all thermal and mechanical properties are summarized in Table S1 in Supporting Information S1), the boundary conditions (V_{ext} = extension rate, V_b = velocity of basal counter flow) and the initial thermal state (red lines). Location and extent of features that promote strain localization at the beginning of extension are indicated: initial temperature anomaly (notch in the 1330°C isotherm) and strain inheritance. The inset displays a close-up view of the upper 130 km of the model, and the strength envelopes (calculated for an average strain rate of 2.84×10^{-16} s^{-1}) of the two different rheologies considered in our models, which differ in the strength of the lower crust (R1 = high crustal strength, R2 = intermediate crustal strength). (c) Temporal evolution of the models: The models have a total duration of 40 Myr and syn-rift duration depends on the extension rate (7.5, 15, 30 Myr).

2.2. Setup and Boundary Conditions for Fantom

Fantom is a thermomechanically coupled, arbitrary Lagrangian-Eulerian, finite-element code that solves for plane-strain, incompressible, visco-plastic creeping flows, and heat transfer in the model domain. Viscous deformation is approximated by nonlinear power law creep and material properties are based on flow laws of wet quartz (Gleason & Tullis, 1995), dry Maryland diabase (Mackwell et al., 1998), and wet olivine (Karato & Wu, 1993). Frictional-plastic deformation is modeled using a pressure-dependent Drucker-Prager yield criterion, considering the effect of plastic strain-weakening on the materials (Huismans & Beaumont, 2003). A full explanation of the inherent equations and a table of all material constants is given in Section S1 and Table S1 in Supporting Information S1.

The model domain is 1,200 km wide, 600 km deep, and vertically stratified (Figure 2b). From top to bottom the model consists of continental crust (0–35 km), lithospheric mantle (35–120 km), and sublithospheric mantle (120–600 km). To test the sensitivity of the model to different crustal strengths, we discern two different crusts, R1, strong crust, and R2, intermediate strength crust (see strength envelopes in the inset of Figure 2b). R1 uses dry Maryland diabase as material for the lower crust, R2 uses wet quartz for the lower crust. Otherwise, the two rheologies consist of the same materials, using wet quartz as material for the upper parts of the crust and wet olivine for the lithospheric and sublithospheric mantle. To account for stronger, melt-depleted conditions, the

flow law of the lithospheric mantle is scaled by a factor 5. We do not consider models with an even weaker crust (see, for instance, Huismans & Beaumont, 2011; Theunissen & Huismans, 2019), because very weak crust does not result in significant rift initialization for the extension durations that we consider. Material that is eroded and deposited as sediment during the model run (materials S1, S2 and S3 in Figure 2b) has the same mechanical properties as upper crust.

We use a 400 km wide area in the center of the model with initial strain inheritance (Figure 2b), simulating inherited structures from previous tectonic events (Theunissen & Huismans, 2019). To localize rifting in the center of this domain, we add a small thermal anomaly at the base of the lithosphere in the center of the model (Figure 2b). A more detailed explanation of the approach for strain inheritance can be found in Supporting Information.

On each side of the model, the lithosphere is extended with half the extension rate as horizontal velocity boundary condition (V_{ext} in Figure 2b). Lateral outflow of material is balanced by a low velocity inflow of material in the sublithospheric mantle in order to preserve mass (V_b in Figure 2b). The bottom and sides of the model are horizontal and vertical free slip boundaries, respectively, whereas the top of the model serves as free surface subject to erosion and deposition. As thermal boundary condition the base of the model is kept at a constant temperature of 1522°C, the lateral boundaries are thermally insulated. The numerical resolution in our models is 500 m horizontally and the vertical resolution is depth dependent with a 200 m resolution in the upper 20 km. This high resolution allows investigating the basin-scale feedback of tectonics and surface processes.

2.3. Setup and Boundary Conditions for FastScape

We use a modified version of FastScape to model surface processes (Braun & Willett, 2013; Yuan et al., 2019). Fastscape accounts for onshore erosion, sediment transport, and deposition in the marine part of the landscape. The rate of change of elevation ($\partial h/\partial t$) in the parts of the landscape above sea level is simulated by solving the stream power law (i.e., river incision; Whipple & Tucker, 1999), and hillslope processes (Culling, 1963):

$$\frac{\partial h}{\partial t} = U - k_f A^m S^n + k_C \nabla^2 h, \quad \text{for } h \geq h_{\text{sea level}} \tag{1}$$

where h is elevation, U is uplift rate, k_f is fluvial erodibility, A is upstream drainage area, S is slope, m and n are stream power law exponents, and k_C is the transport coefficient of hillslope diffusion. We do not include continental deposition. Hence, no material is deposited above sea level and all eroded material is transported by the rivers to the marine domain or out of the model according to the drainage organization.

Below sea level, sediment transport and deposition are simulated using a diffusion equation as described in Yuan et al. (2019). Using the amount of sediment flux coming from the continental domain of the model (Q_s), the rate of elevation change can be approximated by:

$$\frac{\partial h}{\partial t} = k_M \nabla^2 h + Q_s, \quad \text{for } h < h_{\text{sea level}} \tag{2}$$

where k_M is the marine diffusion coefficient. Equation 3 is valid if the material transported below consists of one grainsize. In our case, we consider two different grainsizes and use a coupled-diffusion with distinct transport coefficients for the two grainsizes (having values of 200 and 100 m^2/yr, respectively). We refer to the paper of Yuan et al. (2019) for further technical details about this approach.

FastScape truly sits on top of Fantom and has the same spatial dimension of 500 m. We choose an along-strike extent of 300 km for the FastScape model, resembling a typical width of a continental rift system. The left and right-side boundaries of the landscape are open so that water flows out and the top and bottom boundaries are periodic.

2.4. Modeling Strategy

To investigate the variability of tectonic and surface processes in continental rifts, we test the sensitivity of our models to crustal rheology, extension rate, and fluvial erodibility. The resulting parameter combinations yield 14 different models (Table 1).

Table 1
Summary of Parameters of the 14 Models With Varying Tectonic Parameters (Rheology, Extension Rate) and Erodibility (k_f Value)

Model name	Rheology	Extension rate (km/Myr)	k_f value ($m^{0.2}$/yr)	Evolution displayed in
M1	R1	10	0.5×10^{-5}	Figure 3 Animation 1
M2	R1	5	0.5×10^{-5}	Figure 4 Animation 2
M3	R2	10	0.5×10^{-5}	Figure 5 Animation 3
M4	R1	5	0.25×10^{-5}	Figure 6 Animation 4
M5	R1	5	1.0×10^{-5}	Figure 6 Animation 5
SM1	R1	2.5	0.5×10^{-5}	Animation 6
SM2	R2	2.5	0.5×10^{-5}	Animation 7
SM3	R1	5	0.1×10^{-5}	Animation 8
SM4	R2	5	0.1×10^{-5}	Animation 9
SM5	R2	5	0.25×10^{-5}	Animation 10
SM6	R2	5	0.5×10^{-5}	Animation 11
SM7	R2	5	1.0×10^{-5}	Animation 12
SM8	R1	10	0.25×10^{-5}	Animation 13
SM9	R1	10	1.0×10^{-5}	Animation 14

Note. R1 refers to strong crust, R2 to intermediate strength crust, see also Figure 2b. Detailed analyses of the evolution of structures and topography for the main models (M1–M5) are provided in Figures 3–6. Supplementary models (SM1–SM9) are used to additionally investigate the evolution of the sediment flux for a wider parameter space (Figure 7–9).

We consider two different crustal rheologies (R1 and R2; Figure 2b) with a total 75 km of extension. This is sufficient to develop a rift without reaching crustal breakup. The duration of extension depends on the extension rate and we consider four combinations of extension rate and duration: 7.5 Myr at a rate of 10 km/Myr, 15 Myr at a rate of 5 km/Myr, and 30 Myr at a rate of 2.5 km/Myr. All models have a total duration of 40 Myr with variable durations of the syn- and post-rift phases (Figure 2c).

Fluvial incision controls the erosional efficiency, erosion rate, and sediment yield. In the Stream Power Law, coefficients m and n are relatively well known (Stock & Montgomery, 1999), but fluvial erodibility (k_f) spans a wide range as it incorporates effects related to climate, rock type, vegetation, and abrasive agents (Stock & Montgomery, 1999). We keep $m = 0.4$ and $n = 1$ and test the effect of erosional efficiency by changing fluvial erodibility, considering k_f values of 0.1, 0.25, 0.5, and 1×10^{-5} $m^{0.2}$/yr (Table 1). These values cover a wide range, leading to very little erosion and a long-lasting landscape or very efficient erosion and rapid degradation of the landscape. This can be envisioned as rifts experiencing arid to humid climatic boundary conditions. We use a reference k_f value of 0.5×10^{-5} $m^{0.2}$/yr for all of our extension rates and rheologies (Table 1). To account for preexisting relief, we set the sea level to −1,000 m below the initial model surface (which is at 0 m).

We analyze the output from both the tectonic and surface processes models (see Section S4 in Supporting Information S1 for details of analyses procedure). We focus on five models (models M1–M5 in Table 1), for which we provide detailed analyses of the structural and topographic evolution (Figures 3–6). Supplementary models (SM1–SM9) are included in the analyses of the evolution of topography and sediment flux (Figure 7–9). For all models we provide animations of topography and structures in Supporting Information S1.

3. Results

We provide a detailed description of the evolution of the rift geometry for selected models (M1–M5, Table 1). We focus on the reference model M1 and highlight changes in the evolution of rifting. We then describe the sensitivity of the evolution of elevation and sediment production to extension rate and erodibility.

3.1. Evolution of Rift Geometry and Faults

3.1.1. Reference Model M1

The reference model has a high crustal-strength (rheology R1; Figure 2b), intermediate erodibility ($k_f = 0.5 \times 10^{-5}$ $m^{0.2}$/yr), and an extension rate of 10 km/Myr for 7.5 Myr.

At 3 Ma two boundary faults (F1 and F2) form a 75 km wide asymmetric rift (Figure 3a). Major fault F1 (with approximately 6 km displacement) forms a crustal-scale shear-zone cutting into the upper mantle lithosphere (Figure 3a) and is associated with significant rift shoulder elevation, approximately 3,000 m (Figure 3b). Fault F2 exhibits only approximately 0.6 km displacement and is associated with more subdued topography (Figure 3a). Minor fluvial valleys, orthogonal to the main drainage divides, form on both sides of the rift.

At 6 Ma, displacement along F1 and F2 reaches 10.8 and 6.4 km respectively (Figures 3a and 3b), new fault F4 dissects the footwall of F2, and deformation shifts to the center of the rift forming faults F3 and F5 (Figure 3a). Footwall uplift of F4 reduces the area draining toward the rift basin on the left rift flank. Erosion of the right rift flank is associated with headward migration of the drainage divide. Material eroded from both rift flanks is deposited in the hanging wall grabens of F1 and F2. Activity of F1 ceases at 6.5 Ma with a total offset of 10.8 km, while F2 remains active until 7.5 Ma with a total offset of 7.3 km (Figure 3b).

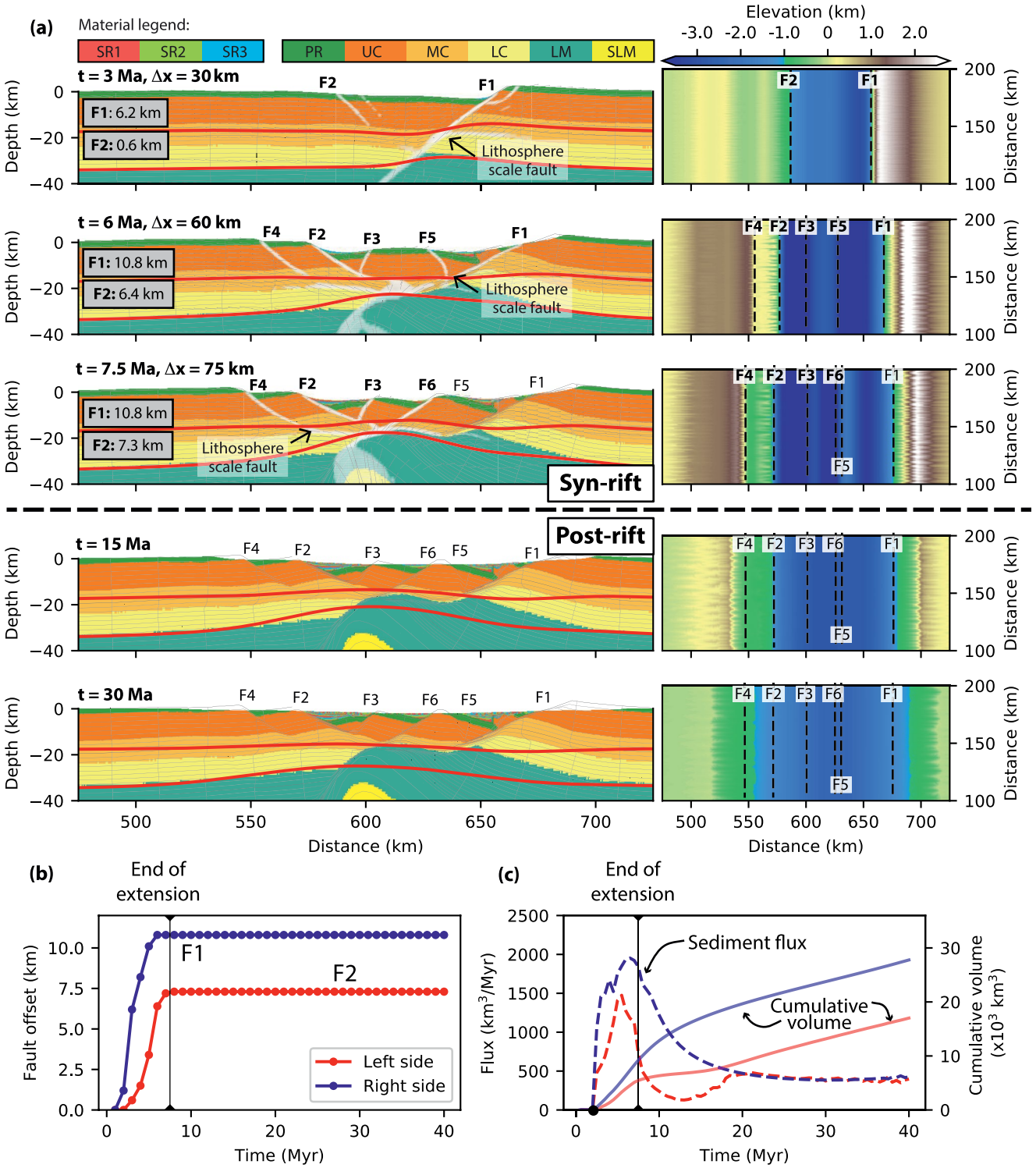

Figure 3. Results of the reference model M1. Model results for model M1 with high crustal strength, 7.5 Myr of extension (extension rate of 10 km/Myr) and intermediate erodibility ($k_f = 0.5 \times 10^{-5}$ $m^{0.2}$/yr): (a) Structures (left column) and topography (right column) at selected time steps. Major faults are labeled in accordance with their onset of activity (faults active during the respective timestep are labeled in bold). Numbers in the gray boxes indicate vertical fault offset on the two boundary faults (F1 and F2). The black arrows indicate lithosphere-scale faults that reach a depth over 15 km. The topography transitions from onshore to offshore at the sea level (−1,000 m). (b) Evolution of the vertical fault offset on the two boundary faults F1 (blue, right side) and F2 (red, left side). (c) Evolution of incremental (dashed curves) and cumulative (solid curves) sediment volumes from the two rift sides over time (blue = right side, red = left side).

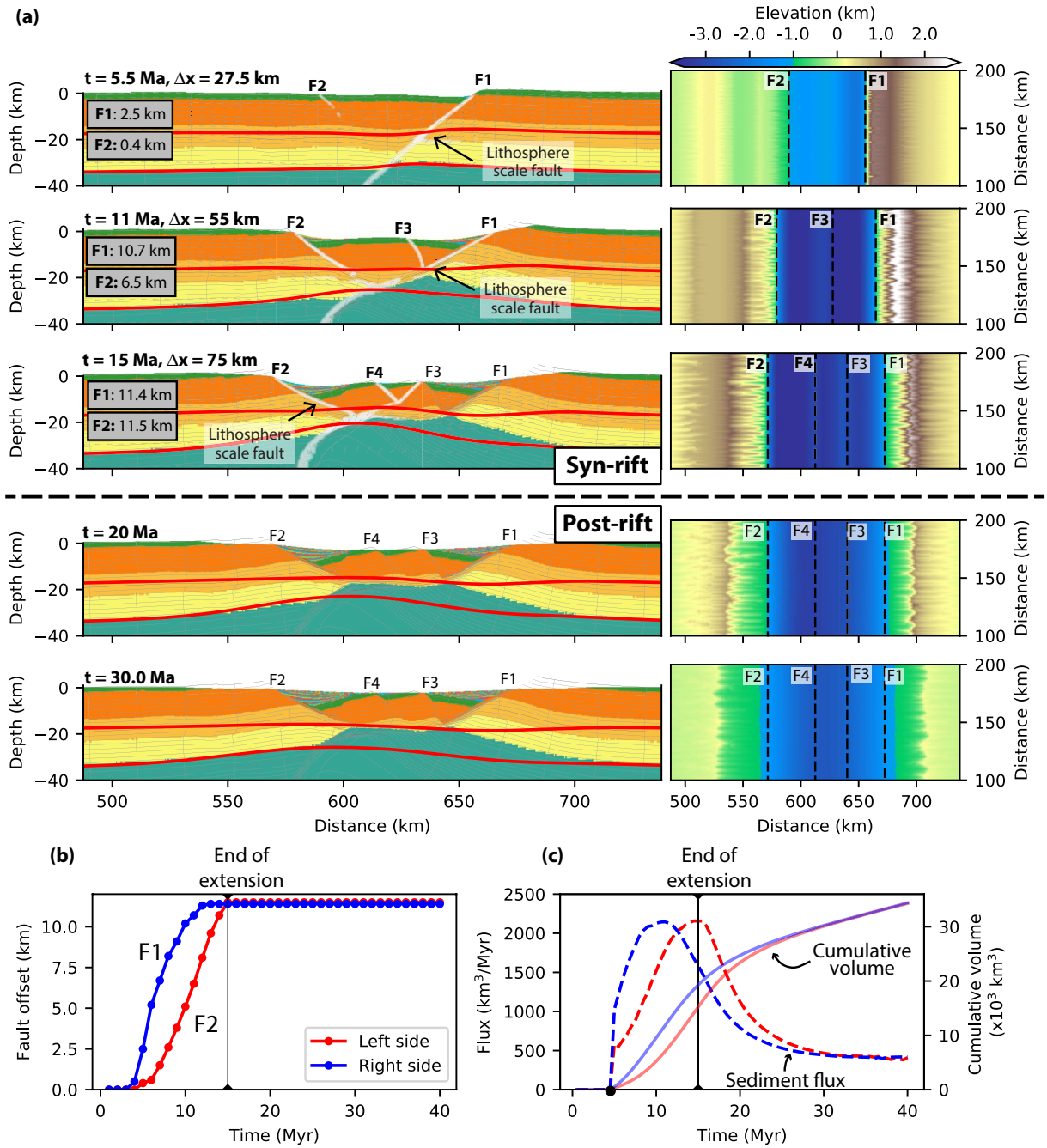

Figure 4. Effect of decreasing the extension rate. Results for model M2 with high crustal strength, 15 Myr of extension (extension rate of 5 km/Myr) and intermediate erodibility ($k_f = 0.5 \times 10^{-5}$ m$^{0.2}$/yr): (a) Structures (left column) and topography (right column) at selected time steps. Major faults are indicated and labeled in accordance with their onset of activity (faults active during the respective timestep are labeled in bold). Numbers in the gray boxes indicate vertical fault offset on the two boundary faults (F1 and F2). The black arrows indicate lithosphere-scale faults that reach a great depth (>15 km). The topography transitions from onshore to offshore at the sea level (−1,000 m). (b) Evolution of the vertical fault offset on the two boundary faults F1 (blue, right side) and F2 (red, left side). (c) Evolution of incremental (dashed curves) and cumulative (solid curves) sediment volumes from the two rift sides over time (blue = right side, red = left side).

At 7.5 Ma deformation is partitioned between left flank faults F2 and F4 and the center of the rift F3 and F6 (Figure 3a). The final rift geometry is asymmetric with the highest offset and topography associated with F1 on the right side (Figure 3a). On the left side, rift topography is associated with F4, whereas the fault block between F2 and F4 forms a low-lying fluvial plain (Figure 3a).

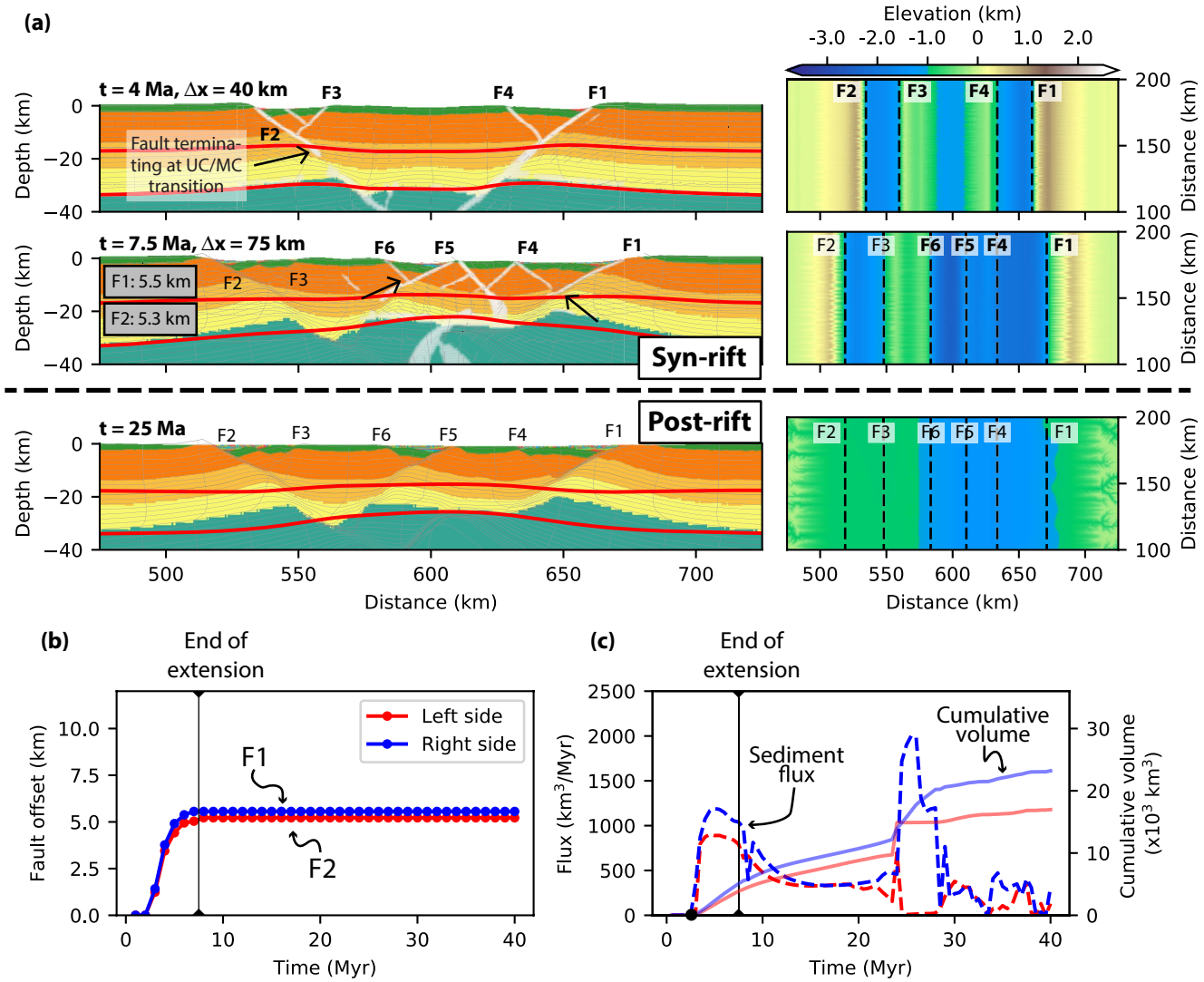

Figure 5. Effect of decreasing crustal strength. Results for model M3 with intermediate crustal strength, 7.5 Myr of extension (extension rate of 10 km/Myr) and intermediate erodibility ($k_f = 0.5 \times 10^{-5}$ m$^{0.2}$/yr): (a) Structures (left column) and topography (right column) at selected time steps. Major faults are indicated and labeled in accordance with their onset of activity (faults active during the respective timestep are labeled in bold). Numbers in the gray boxes indicate vertical fault offset on the two boundary faults (F1 and F2). The black arrows indicate faults that terminate at the transition from upper (UC) to middle crust (MC). The topography transitions from onshore to offshore at the sea level (which is at −1,000 m). (b) Evolution of the vertical fault offset on the two boundary faults F1 (blue, right side) and F2 (red, left side). (c) Evolution of incremental (dashed curves) and cumulative (solid curves) sediment volumes from the two rift sides over time (blue = right side, red = left side).

At 15 Ma both rift flanks are significantly eroded down to approximately 1 km elevation (Figure 3a). Landward drainage divide retreat forms wide low-lying floodplains allowing transit of sediments to the rift that first fill up the marginal rift bounding half grabens and then the central, axial part of the rift (Figure 3a). At 30 Ma, onshore rift flank morphology has been further down warped, and the marginal floodplains and the rift axis are submerged (Figure 3a).

Sediment flux varies strongly throughout the model evolution (Figure 3c). On the right side of the rift sediment flux reaches a maximum value of 2,000 km^3/Myr around the end of activity of F1 at approximately 6.5 Ma (Figure 3c) and then decreases exponentially to a steady value at 25 Ma (Figure 3c). On the left rift side, the sediment flux peaks earlier and at a lower value approximately 1500 km^3/Myr and then similarly decreases exponentially during the post rift. The contrasting evolution of sediment flux through time is also reflected in the cumulative sediment volumes, 17×10^3 and 28×10^3 km^3 at 40 Ma for the left and right side, respectively (Figure 3c).

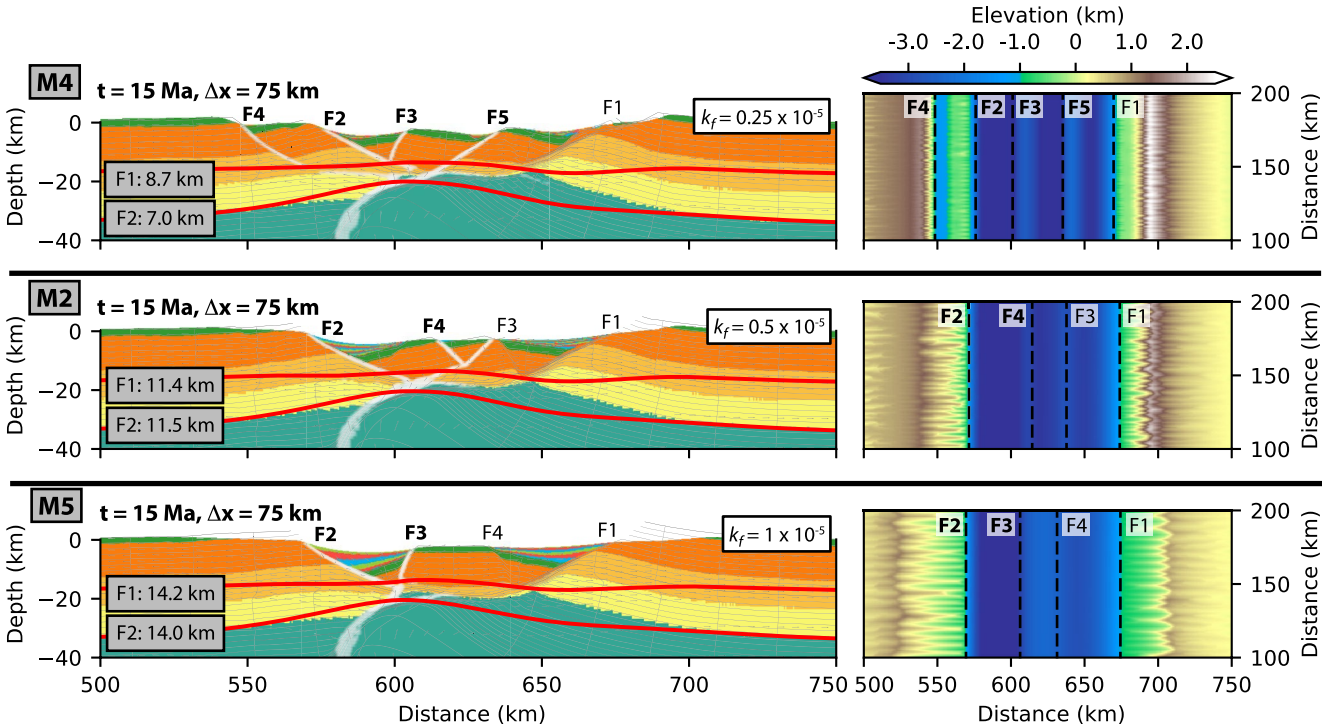

Figure 6. Sensitivity to erodibility. Structures (left column) and topography (right column) at the end of extension at 15 Ma for models M2, M4, and M5 with high crustal strength, 15 Myr of extension and variable erosional efficiency: (a) M4 with $k_f = 0.25 \times 10^{-5}$ m$^{0.2}$/yr, (b) M2 with $k_f = 0.5 \times 10^{-5}$ m$^{0.2}$/yr, and (c) M5 with $k_f = 1 \times 10^{-5}$ m$^{0.2}$/yr. Faults are labeled according to their onset of activity, and active faults at 15 Ma are labeled in bold. Numbers in the gray boxes indicate vertical fault offset on the two boundary faults (F1 and F2). The topography transitions from onshore to offshore at the sea level (−1,000 m). Flank erosion, and thick, tilted sediment wedges.

3.1.2. Effect of Decreasing Extension Rate

Model M2 (Figure 4) uses half the extension rate of the reference model M1 (5 km/Myr until 15 Ma) and identical other parameters (high crustal-strength rheology R1, intermediate erodibility $k_f = 0.5 \times 10^{-5}$ m$^{0.2}$/yr). Slower extension in M2 delays localization of deformation and rift formation with respect to reference model M1.

At 5.5 Ma, an asymmetric rift has developed with 2.5 km of offset on right boundary rift fault F1 and rift flank elevation of ∼1500 m, and an incipient fault F2 on the left side (Figures 3a and 3b). With ongoing extension both F1 and F2 take up most of the deformation leading to a largely symmetric rift at 11 Ma. Activity on F1 ceases around approximately 13.5 Ma, whereas F2 remains active until the end of extension at 15 Ma. Subsequently, deformation shifts basin ward breaking up the central block between F1 and F2, forming conjugate faults F3 and F4 in the center. In contrast to model M1 most of the deformation is accommodated by the rift boundary faults F1 and F2 with a similar total offset (approximately 11.5 km) at the end of extension (Figure 4b). Sediment flux peaks are similar in magnitude on both sides of the rift and coincide with the timing of cessation of activity on F1 and F2 (Figure 4c). Cumulative sediment volume at 40 Ma is higher than in model M1 reaching the same magnitude on both rift sides (Figure 4c).

3.1.3. Effect of Decreasing Crustal Strength

Model M3 (Figure 5) investigates the influence of intermediate crustal strength (rheology R2), lower than in the reference model M1, with the same extension rate (10 km/Myr), and erodibility ($k_f = 0.5 \times 10^{-5}$ m$^{0.2}$/yr).

Intermediate crustal strength results in a significantly different rift style compared to models M1 and M2, with more distributed deformation. At 4 Ma and 40 km extension, a broad 150 km wide, symmetric graben has formed with equal offset on main rift boundary faults F1 and F2, and secondary hanging wall faults F3 and F4 antithetic to the main rift boundary faults (Figure 5a). Offset along F1 and F2 leads to a maximum rift flank elevation of approximately 1500 m, lower compared to models with strong crustal rheology. Moderate footwall uplift along

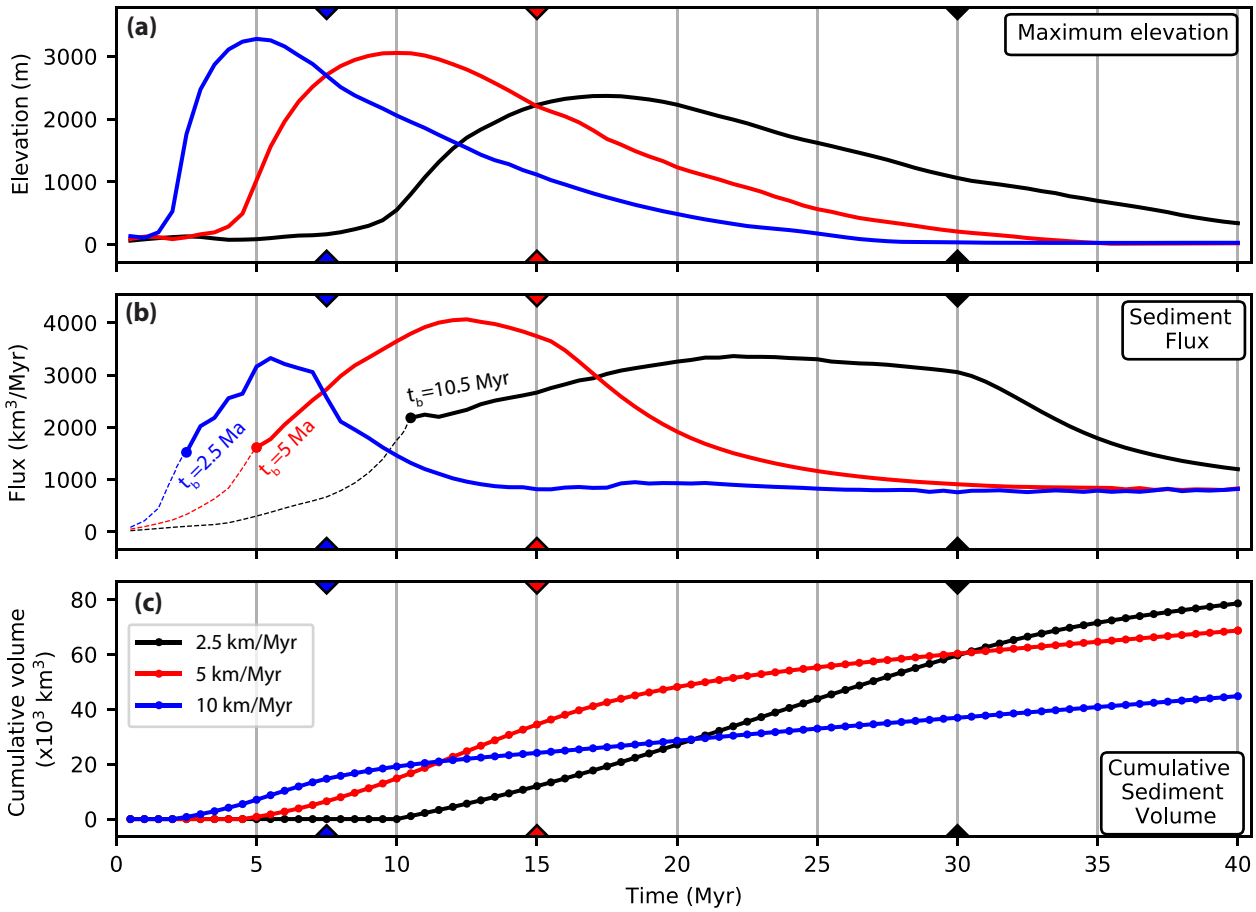

Figure 7. Influence of extension rate on the evolution of elevation (a), sediment flux (b), and sediment volume (c). Results are for models M1, M2, SM1 with high crustal strength, intermediate erosional efficiency ($k_f = 0.5 \times 10^{-5}$ m$^{0.2}$/yr), and variable extension rates/extension durations of 30 Myr (black), 15 Myr (red), and 7.5 Myr (blue). In all panels, the colored triangles indicate the end of extension of the respective model. Note that sediment flux in the slowest model (2.5 km/Myr) does not reach a steady value within the 40 Myr simulation. Sediment flux and volume are only recorded after the basin has reached sea level at time t_b (which depends on the respective extension rate). Prior to t_b sediment is transported out of the model domain. The total volumes of sediment lost this way are 4,952, 2,016, 904, and 322 km^3 for models with extension rates of 2.5, 5, 10, and 15 km/Myr, respectively.

secondary hanging wall faults F3 and F4 divides the graben into three sub-basins. At 7.5 Ma major bounding faults F1 and F2 accommodate offsets approximately 5.5 km, significantly less compared to models 1 and 2 (Figure 5a). At this stage deformation has migrated to the right half graben breaking up its hanging wall forming second-generation normal faults F4, F5, and F6 resulting in a broad about 3,000 m deep submerged basin. Hanging wall subsidence associated with F2 results in a separate shallow submerged basin. Post-rift erosion efficiently removes the rift shoulders leading to head-ward erosion, drainage divide migration, and river capture events around 25 Ma (Figure 5a). Sediments are deposited in the half-grabens associated with F1, F2, and F5 leading to rapid infill and a shallow basin at the end of the model at 40 Ma.

Sediment flux (Figure 5c) varies strongly throughout the model evolution. Peaks from both the left (900 km^3) and right (1,250 km^3) side occur at approximately 6 Ma, coeval with the end of main activity on F2 and F1, respectively (Figure 5b). On the right rift side, a significant peak in sediment flux (approximately 2,000 km^3) during the post-rift is observed at 25 Ma, related to river capture on the right rift flank. The horst uplifted between F3 and F6 (Figure 5a) forms a transient, topographic barrier. This prevents the sediment coming from the left rift side from reaching the central basin, resulting in decreased sediment flux from the left rift side during 25–30 Ma, also reflected in the difference of the cumulative volume of 12×10^3 and 22×10^3 km^3 for the left and right side, respectively.

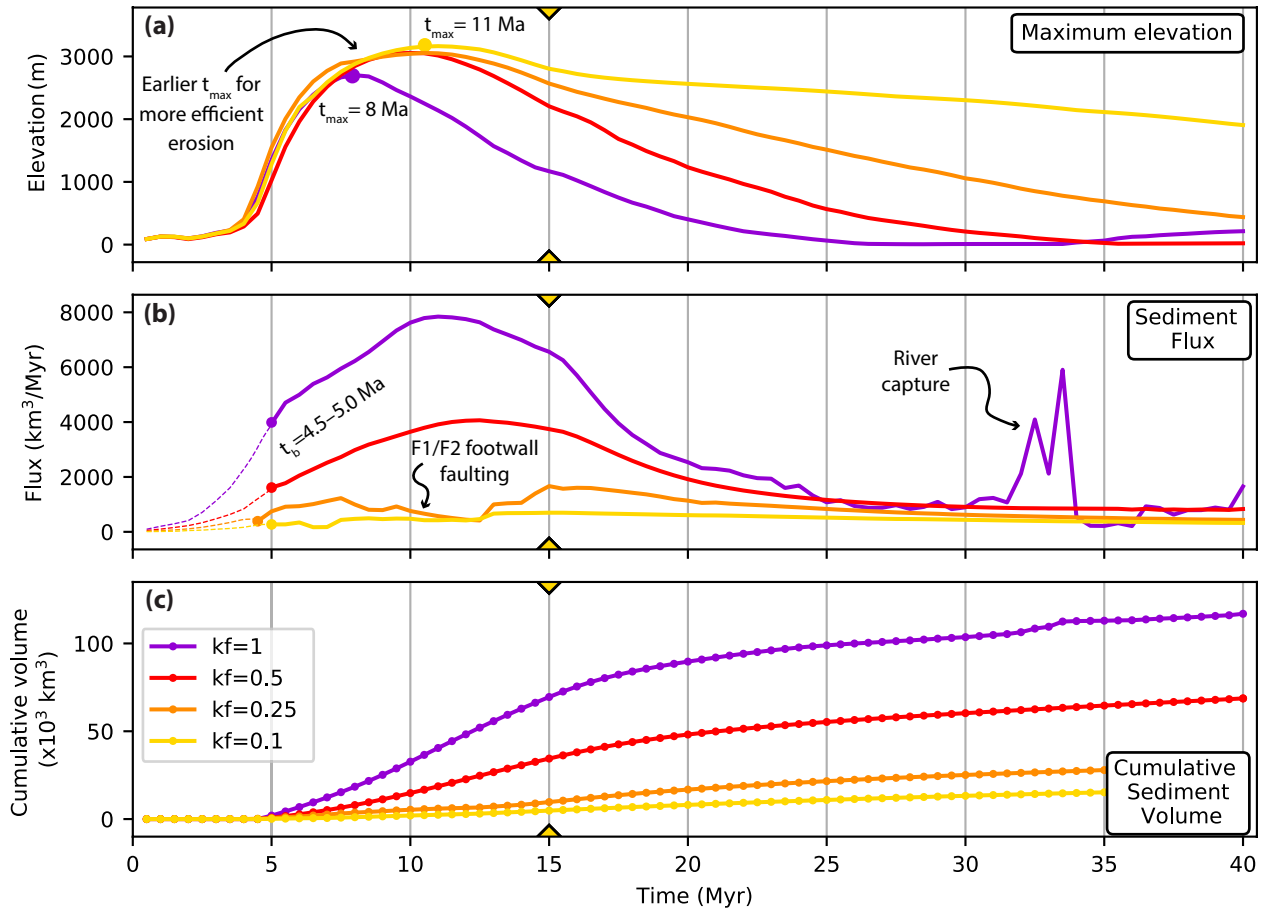

Figure 8. Influence of erosional efficiency on the evolution of elevation (a), sediment flux (b) and sediment volume (c). Results for models with high crustal strength, 15 Myr of extension and variable erosional efficiencies of $k_f = 0.1 \times 10^{-5}$ m$^{0.2}$/yr (yellow), $k_f = 0.25 \times 10^{-5}$ m$^{0.2}$/yr (orange), $k_f = 0.5 \times 10^{-5}$ m$^{0.2}$/yr (red), and $k_f = 1 \times 10^{-5}$ m$^{0.2}$/yr (purple). In all panels, the yellow triangles indicate the end of extension of the models. In panel (a), t_{max} refers to the timing of maximum elevation, which occurs earlier for more efficient erosion. Sediment flux and cumulative sediment volume are only recorded after the basin of the respective model has reached sea level at time t_b (which varies between 4.5 and 5 Ma). Prior to t_b sediment is transported out of the model domain. The total volumes of sediment lost this way are 3,358, 2,016, 726, and 393 km^3 (for models with k_f values of 1, 0.5, 0.25, and 0.1×10^{-5} m$^{0.2}$/yr, respectively). Note that sediment flux in model with low erosional efficiency $k_f = 0.25 \times 10^{-5}$ m$^{0.2}$/yr exhibits several maxima and minima, due to fault activity in the footwalls of F1 and F2, which lead to drainage reorganization (see Figure 6).

3.1.4. Effect of Erodibility

Models M4, M2, and M5 (Table 1) explore the sensitivity to changing erodibility with k_f values 0.25, 0.5, and 1×10^{-5} m$^{0.2}$/yr, respectively. All three models have a high crustal-strength rheology R1 and low extension rate 5 km/Myr. We compare the models at the end of extension at 15 Ma (e.g., Figure 6; see Supporting Information S1 for full model evolution).

Varying erodibility affects both the number and the offset of faults. Model M4 with very low erodibility exhibits five faults and minor rift flank erosion. In contrast model M2 with intermediate erodibility is dominated by two main rift boundary faults and moderate rift flank erosion. Model M5 with even higher erodibility shows strongly enhanced offset along F1 and F2 (>14 km), significant rift.

Erodibility also strongly impacts the topography through the drainage system. Low erodibility model M4 develops numerous small catchments with a drainage divide at approximately 30 km from the shoreline, whereas the high erodibility model M5 develops fewer larger catchments and a drainage divide that migrates to approximately 55 km from the shoreline (Figure 6). Rift shoulder elevation is lowered faster for higher erodibility (<1,500 m at 15 Ma) than for lower erodibility (2,000–2,500 m at 15 Ma).

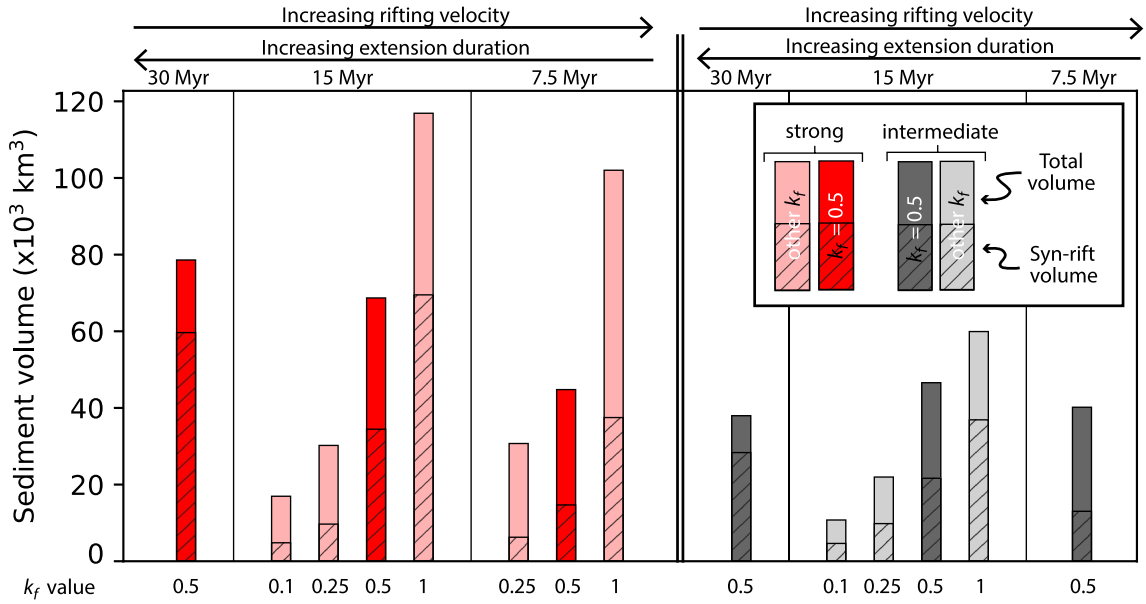

Figure 9. Sediment volumes generated during rifting. Comparison of the sediment volumes (deposited since the basin has reached sea level) for the 14 models (Table 1). Models are grouped according to their rheology (red = strong, R1; gray = intermediate, R2) and subsequently ordered with respect to extension duration/rate. Models with dark-colored bars share the same k_f value (i.e., $k_f = 0.5$), in order to easily compare the sediment volumes for models with the same intermediate erosional efficiency. Models with other k_f values (i.e., 0.1, 0.25, and 1) are pale colored. For each model, the height of the bar indicates the total sediment volume, whereas the height of the hatched bar indicates the synrift volume.

3.2. Sensitivity of Elevation and Sediment Production to Extension Rate and Erodibility

We next explore how varying extension rate and erodibility affect elevation and sediment production. Models SM1, M1 and M2 (Table 1) explore the sensitivity to varying extension rates, equal to 2.5, 5, and 10 km/Myr, respectively, for identical erodibility $k_f = 0.5 \times 10^{-5}$ m$^{0.2}$/yr and crustal strength R1 (Figure 7). In contrast, models M4, SM3, M2, and M5 (Table 1) explore the effect of varying erodibility with $k_f = 0.1, 0.25, 0.5, 1 \times 10^{-5}$ m$^{0.2}$/yr, respectively for an identical extension rate 5 km/Myr and crustal strength R1 (Figure 8).

Maximum elevation follows a similar evolution for the models with variable extension rate with four characteristic phases (Figure 7a). During Phase 1, initial rifting with distributed deformation generates almost no topography. Maximum topography increases rapidly during Phase 2 when deformation localizes, and the main rift shoulders are uplifted (Figure 7a). Maximum elevation is reached systematically before the respective end of extension. The faster the extension rate, the earlier the peak, which is also slightly higher (Figure 7a). During Phase 3, rift activity migrates to the center of the basin, with maximum topography slowly decreasing toward the end of the syn-rift phase. After the end of extension, during Phase 4, elevation decays gradually and the rift shoulders are completely eroded away with a timescale depending primarily on fluvial erodibility (Figures 7a and 8a).

Sediment flux similarly exhibits four characteristic phases in the models (Figure 7b). Initial Phase 1 shows a slow increase of sediment flux with time. During Phase 2 sediment flux increases rapidly after the basin reaches sea level (time t_b), and reaches a peak shortly after maximum topography is reached. Subsequently sediment flux decreases slowly during Phase 3 until the end of extension (Figure 7b). The timing of peak sediment flux depends on the extension rate (Figure 7b). During Phase 4 the sediment flux decreases exponentially to a steady state value 10–15 Myr after the end of extension (Figure 7b). The cumulative sediment volumes increase slowly with time, and at 40 Myr cumulative sediment volumes are notably higher for lower extension rates (Figure 7c).

Models with varying erodibility (e.g., Figure 8) show features similar to those with varying extension rate. All reach a maximum elevation of approximately 3,000 m except for the high erodibility model that has maximum topography approximately 2,800 m (Figure 8a). The timing of maximum topography occurs earlier with increasing erodibility and occurs, in all cases, well before the end of extension. Subsequently, during the post-rift maximum elevation decreases progressively to a few hundreds of meters (Figure 8a).

Maximum sediment flux is proportional to erosional efficiency (Figures 8b and 8c). Models with varying erosional efficiency exhibit maximum sediment flux values of about 800, 1,800, 4,000, and 8,000 km^3/Myr, respectively, for k_f ranging [0.1, 0.25, 0.5, 1.0] $\times$ 10^{-5} m$^{0.2}$/yr. Maximum sediment flux is systematically later than peak elevation. The case with high erodibility ($k_f = 1.0 \times 10^{-5}$ m$^{0.2}$/yr) shows a sudden increase in sediment flux (>6,000 km^3/Myr) at approximately 33 Ma, marking a river capture event (Figure 8b). Cumulative sediment volume at 40 Ma increases with erodibility (from 20 to 120 $\times$ 10^3 km^3; Figure 8c).

4. Discussion

In the following, we first discuss the first-order controls of rheology, extension rate, and surface process efficiency on the evolution of modeled rifts. Next, we address how the different factors are reflected in the sediment production and compare with natural rift examples. We then discuss limitations of our modeling approach and compare our results to other modeling studies.

4.1. Influence of Extension Rate, Rheology, and Erodibility on Rift Evolution

Our results show that the evolution of a rift is mostly controlled by the degree of strain localization. High degree of strain localization results in a simpler rift geometry, with fewer active faults and greater fault offset. Models M1 to M5 demonstrate how crustal rheology, surface process efficiency, and extension rate affect the degree of strain localization.

Comparison between model M1 with strong crust (Figure 3) and M3 with intermediate crustal strength (Figure 5) illustrates the effect of rheology on strain localization. Intermediate crustal strength limits the coupling between crust and mantle (Beucher & Huismans, 2020), and results in faults terminating at the top of the viscous middle crust (Figure 5). The weaker coupling reduces strain localization and leads to a wide symmetric rift with multiple active faults with moderate fault offset. In contrast, strong crust promotes strain localization in a narrow rift with few large offset crustal-scale faults that connect to the strong upper mantle lithosphere (Figures 3 and 4). Rift flank topography associated with footwall uplift is directly controlled by the amount of fault offset and by the strength of the crust. The strong crust cases promote large offset normal faults that generate high topography (>3,000 m), while in contrast intermediate crustal strength cases promote reduced offset and lower rift flank topography (approximately 1,500 m).

The relative importance of tectonic uplift and erosion in the models can be understood considering the nondimensional uplift-erosion number N_e (Whipple & Tucker, 1999) that can be formulated for $n = 1$ as $N_e \propto U / (k_f \times h)$, where U is tectonic uplift rate, and h is elevation. N_e only weakly scales with drainage area or river length, which are therefore omitted. This simple relationship shows that for large N_e uplift dominates over erosion, and vice versa for low N_e. We observe in our models that halving the extension rate (which reduces the uplift rates) has the same effect as doubling k_f, both in terms of structure and sediment flux. This is easy to explain with N_e, because the resulting erosion number N_e will be the same when either halving the extension rate or doubling k_f. Similarly, models with strong rheology result in higher topography (3000 m) than those with intermediate rheology (1500 m). Accordingly, if we choose an intermediate rheology, we need to either half the extension rate, or double k_f in order to obtain a similar N_e, that is, the same surface process efficiency.

The behavior of models M1, M2, M4, M5 is consistent with this simple scaling of the trade off and relative importance of extension rate that controls rock uplift rates along the main rift bounding faults and of fluvial erodibility that controls the rate of erosion of topography generated along these faults, counteracting rock uplift. Models M1 (fast extension, Figure 3) and M2 (slow extension, Figure 4), with an identical erodibility, show that slower extension promotes localization of deformation with only four active faults in model M2 with higher offset as compared to six faults in model M1. In contrast Models M2, M4, and M5 (Figure 6) illustrate the effect of varying erodibility for an identical extension rate. Higher erodibility promotes strain localization resulting in fewer faults with more offset and more symmetric rifting. Erosional efficiency is increased for either a higher erodibility or for slower extension. A positive feedback between footwall erosion, hanging wall sedimentation, and fault offset has been demonstrated by earlier studies (e.g., Maniatis et al., 2009; Olive et al., 2014; Theunissen & Huismans, 2019). Our models show that a higher erosional efficiency increases this feedback owing to more erosion in the footwall and deposition in the hanging wall. Efficient erosion and deposition promote the evolution of large displacement boundary faults (Figures 4 and 6). The increased offset on the boundary faults delays the

basin-ward migration of deformation and limits the development of other faults. Intermediate crustal strength cases result in lower rift shoulders resulting in lower surface process efficiency given the same k_f value, which limits the feedback between tectonic uplift and erosion.

In summary, rheology, extension rate, and erodibility impact the structural evolution of rifts. For a given erodibility, a stronger crust and slower extension increase strain localization: fewer faults are active, more fault offset is generated, the rift is more symmetric, and the feedback between erosion and deposition is stronger. This, in turn, also has important implications for the evolution of the sediment production of rift systems, further discussed below.

4.2. Sediment Production of the Rift

4.2.1. Total Volume of Sediment

In general, the amount of sediment produced during rifting depends on (a) topography susceptible to erosion, and (b) surface process efficiency. Syn-rift tectonic rock uplift generates elevated rift shoulders and fluvial erosion provides the main source of sediments. During the post-rift, rivers can capture the hinterland drainage network, yielding additional sediment. These two sources of sediment are a function of the evolution of the rift, and the total sediment volume is controlled by rift structural style and rheology, by extension rate, and by erodibility. Figure 9 summarizes the volumes of sediment produced after 40 Myr of simulation for all models (M1 to M5 and SM1 to SM9, Table 1).

As expected, for a strong crust and a given extension rate (for instance for models with 15 Myr of extension), a higher erodibility increases the total sediment volume (Figure 9). However, for a given erodibility, slower extension models with lower topography and rock uplift rates (i.e., 30 and 15 Myr of extension) yield substantially more sediment (70–80 $\times$ 10^3 km^3), than faster extension models with higher topography and rock uplift rates (i.e., 45 $\times$ 10^3 km^3 for 7.5 of extension; Figure 9). This is intuitive, as the volume of generated sediment scales with the magnitude of topography and cumulative rock uplift; the latter is higher for lower extension rates (Figures 3 and 4). Slower extension localizes deformation on fewer structures sustaining more fault offset over a longer duration and can be explained by the more efficient feedback between continued fault localization and surface processes at lower extension rates (Figures 7 and 9).

For intermediate crustal strength, higher erodibility similarly increases the total sediment volume (Figure 9). However, comparison between models with intermediate and high crustal strength shows that cases with stronger crust generate 10%–100% more sediment (e.g., models M1 vs. M3 or M5 vs. SM7, Figure 9). Lower fault offset and associated footwall uplift for the intermediate crustal strength cases limits the feedback between erosion and deformation and the lower maximum elevation of the rift shoulders results in lower sediment volumes.

The amount of syn-rift sediment relative to the total sediment volume increases systematically with increasing erodibility, irrespective of the rheology and extension rate (Figure 9). This effect is stronger for lower rates of extension, as the feedback between erosion/deformation is stronger. For example, models with intermediate extension duration (15 Myr) and erodibility (i.e., models M2, M5 and SM7 with $k_f \geq 0.5 \times 10^{-5}$ $m^{0.2}$/yr), produce over 50% of the total sediment volume during the syn-rift. This results in a rift, where the majority of sediment is deposited during active deformation and where sediment is subjected to faulting.

For the models with very high erodibility (i.e., $k_f = 1 \times 10^{-5}$ $m^{0.2}$/yr), river capture events during the post-rift phase may result in a transient increase of the volume of sediment delivered to the basin. However, the volume of sediment generated by river capture is small compared to that generated during the syn-rift phase (i.e., Figure 8c).

In summary, total sediment volume produced during rift evolution primarily reflects the combined effects of strain localization and erodibility. Slow extension, strong crust, and efficient surface processes yield higher total volumes of sediment. For a given erodibility, a reduction of 50% in the extension rate results in a 15%–40% higher sediment volume (Figure 9). Sediment volume is directly proportional to erodibility (Figure 9). Efficient erosion increases the proportion of syn-rift to post-rift sediments (Figure 9). These observations point toward a complex interaction of tectonic and surface processes controlling sediment production. A rift system may generate a large amount of sediment based on its tectonic boundary conditions (i.e., the degree of strain localization could be

high, because the crust is strong, and extension is slow). Low erosional efficiency may in turn affect the degree of strain localization limiting the feedback between deformation and erosion and reducing sediment production.

4.2.2. Temporal Evolution of Rift Structure, Sediment Flux, and Comparison to Natural Cases

The evolution of rift structure and associated sediment flux (Figure 10a) follows four morpho-tectonic phases (Figure 10b). Phase 1 early-stage rift initiation is marked by distributed deformation, limited offset on several faults that produces little elevation, and low erosion rates, generating little sediment. Phase 2 exhibits localization of deformation on the main rift bounding faults with rapid rift flank uplift, basin subsidence, river incision into the uplifting rift flanks, and steep relief resulting in high erosion rates and a strong increase in sediment flux. Phase 3 basin-ward migration of fault activity, associated with a decrease in uplift and erosion rates, is characterized by sediment flux slowly decreasing from its peak. After the end of extension, decay Phase 4 shows exponential decrease in sediment flux reflecting post rift fluvial erosion of rift flank topography and landward migration of river divides. Drainage capture of the hinterland during Phase 4 may lead to a transient increase in sediment flux. These four phases can be recognized in both strong and intermediate crustal strength models. In the case of intermediate crustal strength, the general trend of the flux is similar, but the magnitude of the different peaks is lower compared to the high crustal strength case (Figures S4 and S5 in Supporting Information S1).

We suggest that the phases of rifting shown by our models reproduce many characteristics of natural rift systems. Phases 1 to 3 can be recognized in the northern North Sea (Cowie et al., 2005; Fazlikhani et al., 2021; Fossen et al., 2021), where deformation was initially distributed over several 100s of kilometers of width (e.g., Phase 1), before localizing on the boundary faults that accommodate most of the strain forming a 150 km wide rift (Phase 2), and subsequent basin-ward migration of deformation at the end of the syn-rift (e.g., Phase 3; Cowie et al., 2005; Fazlikhani et al., 2021). Similarly, the Gulf of Suez (Gawthorpe et al., 2003) exhibits both initial distributed deformation (Phase 1), followed by localization of deformation on the boundary faults (Phase 2), and a subsequent basin-ward shift in deformation (Phase 3). The Gulf of Corinth exhibited an initial phase of wide and distributed extension (Phase 1) before deformation shifted into the location of the present-day Gulf (Phase 2/3; Ford et al., 2017; Gawthorpe et al., 2018).

Full coverage of the evolution of sediment flux for the active stages of rifting is scarce for natural examples. However, the Gulf of Suez and Lake Albert rift provide sufficient data coverage and corroborate our proposed pattern. In the Gulf of Suez, the syn-rift peak in sediment flux coincides with the rift climax (Phase 2–3), with a strong decrease to low steady sediment flux in the post-rift (Phase 4), followed by a second, climate-induced peak in sediment flux (Rohais et al., 2016; Rohais & Rouby, 2020). The Lake Albert rift (East African Rift system) exhibits low sedimentation rates during the first 11 Myr of slow extension (Phase 1; Simon, 2015), followed by a strong increase and maximum sedimentation rates during the next 4 Myr, reflecting localization and increased fault offset on the main rift boundary fault (Phase 2). Lastly, a major river capture event, characteristic for Phase 4, explains the increase in sediment flux in the Zambezi Delta of the East Africa rifted margin (Walford et al., 2005).

The BQART method (Syvitski & Milliman, 2007) that empirically relates the present-day sediment flux of modern river systems to relief, catchment area, and climatic factors, is used to invert the evolution of sediment flux to infer the past topographic evolution of rifts (e.g., Rohais & Rouby, 2020; Sømme et al., 2019). Our model results allow independent validation of the BQART method on geologic timescales. We use maximum topography as a measure of relief and compare this to the sediment flux of our models. Peak elevation systematically predates peak sediment flux by 1–3 Myr in models with sufficiently high erosion for a river network to develop (Figures 7 and 8). Delay of peak sediment flux relates to a delay in formation of a well-developed, fluvially created relief after maximum elevation is reached. The magnitude in peak sediment flux correlates strongly with erodibility consistent with the climatic factors in the BQART method. These observations show that long-time scale temporal changes in sediment flux reflect coeval changes in topography, consistent with one of the basic assumptions of the BQART method. However, the magnitude of the peak in sediment flux does not necessarily scale with the magnitude of topography, indicating a complex relationship between the sediment flux and relief/topography. This is in accordance with observations from Brewer et al. (2020) suggesting that relief and paleo-topography are a significant source of uncertainty for estimation of sediment flux with the BQART method. In our models, the magnitude of topography is mostly sensitive to crustal strength and to a lesser degree to extension rate. Both peak sediment flux and cumulative sediment volume are critically dependent on the feedback between erosion, deposition, and fault offset. A system with a strong feedback, that is, slow extension combined with high

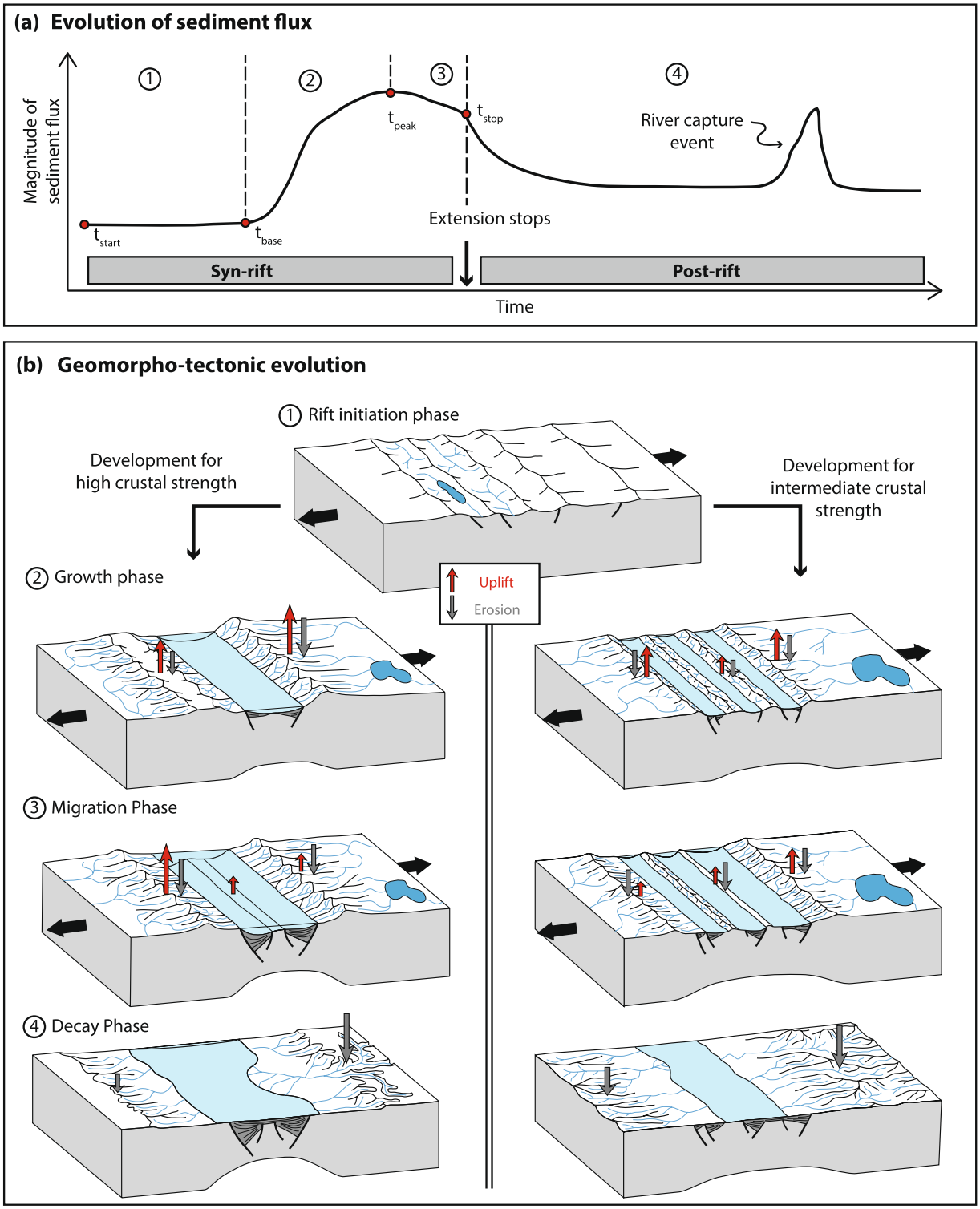

Figure 10. Evolution of the sediment flux related to rifting phases. (a) General evolution of the sediment flux subdivided into four phases, and (b) cartoons of the four geomorpho-tectonic phases of the rift. After an initial phase of distributed deformation (Phase 1), the rifts have a different tectonic and topographic evolution (Phase 2 to 4), depending on the crustal strength: The left column displays the evolution in case of a high crustal strength, the right column in case of intermediate crustal strength. Red arrows indicate the magnitude of rock uplift, and gray arrows the magnitude of erosion, such that if uplift exceeds erosion the surface is uplifting, and when erosion exceeds uplift the surface is lowered.

erodibility, yields more sediment, compared to a system with fast extension, higher rock uplift rates and topography, and a weaker feedback. In natural systems independent constraints on tectonic and climatic boundary conditions and their effect on topography and sediment flux may help to refine the BQART method for reconstructing the topographic evolution of rifts from the sedimentary record. Our results also demonstrate a time lag between peak rock uplift rate, topography, and sediment flux, which is mostly a function of the extension rate (Figures 7 and S3a in Supporting Information S1). If the extension rate is low, peak uplift rate precedes the major pulse in sediment that is delivered to a basin by several million years (e.g., 5 Myr for model M2). This may help to refine the understanding and interpretation of sedimentary records, when it comes to attributing changes in sediment flux to tectonic events.

In summary, the temporal evolution of the sediment flux follows a distinctive pattern. It reflects the successive phases of the tectonic and geomorphic evolution of the rift system, which can also be observed in natural systems. The magnitude of the peak in sediment flux depends on the erosional efficiency, but also on the magnitude of topography as controlled by crustal rheology. The duration of the phases and the timing of the sediment flux peak(s) depend on the extension rate and the erosional efficiency.

4.3. Comparison With Previous Modeling Studies and Limitations of Our Modeling Approach

Earlier studies investigated continental extension using numerical models, emphasizing the evolution of the late stages of rifting or passive margin formation. Several of these studies focused on the role of crustal rheology and surface processes (e.g., Andrés-Martínez et al., 2019; Beucher & Huismans, 2020; Buiter et al., 2008; Theunissen & Huismans, 2019), whereas others focused on the interplay of crustal rheology and extension rate (e.g., Naliboff et al., 2017; Svartman Dias et al., 2015; Tetreault & Buiter, 2018). Our study is the first to test the sensitivity of continental rifting and the associated surface process response to the combined effects of crustal rheology, extension rate, and erodibility, using a fully coupled thermomechanical surface processes model.

Our results corroborate the role of crustal rheology controlling the coupling between crust and mantle, with stronger coupling resulting in more localized deformation (e.g., Theunissen & Huismans, 2019) leading to higher elevation of the rift shoulders (e.g., Beucher & Huismans, 2020; Tetreault & Buiter, 2018). Extension rate and erodibility have a subordinate control on crust-mantle coupling. For a strong coupling, we observe asymmetric rifts (in terms of fault offset and elevation) during the initial stages of rifting, irrespective of the extension rate. However, in case of slower extension enhanced offset along the second rift bounding fault leads to symmetric rift structure toward the end of extension.

The feedback effect between erosion, sedimentation, and deformation during rifting has been described in earlier studies (Andrés-Martínez et al., 2019; Bialas & Buck, 2009; Buiter et al., 2008; Korchinski et al., 2021; Maniatis et al., 2009; Olive et al., 2014; Theunissen & Huismans, 2019). Also in our case, stronger surface processes lead to more strain localization (Andrés-Martínez et al., 2019), more fault offset and prolonged fault activity (Beucher & Huismans, 2020; Olive et al., 2014; Theunissen & Huismans, 2019) and more symmetric basins with fewer active faults (Buiter et al., 2008). In addition, we show that the feedback of surface processes on tectonics is stronger for slower (but longer duration) extension, resulting in larger fault offset, generating more sediment.

Our models have the following inherent limitations: We do not include temporal or spatial variations of erodibility in our models and 3D effects of deformation are excluded owing to the 2D nature of the thermo-mechanical model. We only consider sedimentation offshore below sea level, and no material is deposited in the continental domain. Thus, any onshore sediment that could be remobilized later on, is not considered in our analysis of the sediment flux or the total sediment volume. No material is deposited during the early stages of rifting before the basin has reached sea level and sediment produced during this time leaves the model domain. However, not including the sediment generated during early rifting does not significantly change total sediment volume estimates.

5. Conclusions

We use a thermomechanical model coupled with a landscape evolution model to investigate the evolution of continental rifts. Our models aim at resolving the evolution of tectonic activity, the associated topography and sediment production during rifting, and how they are affected by the tectonics and surface processes. We show that the degree of strain localization is critical for the evolution of a rift, and that it is controlled by crustal rheology, extension rate, and erodibility. Our results corroborate that an increase in erodibility promotes a strong coupling between tectonic and surface processes, through the feedback between footwall erosion, hanging wall deposition, and increased fault offset. We demonstrate that for an intermediate crustal strength, weak coupling between crust and mantle limits fault offset, which reduces the efficiency of the feedback. Feedback between tectonics and surface processes is strongest for slower and extended extension owing to lower uplift rates and prolonged fault activity. Slowly extending rift systems with strong crust and efficient erosion exhibit a strong coupling between tectonics and surface processes, resulting in a structurally simple rift, with large fault offset and high sediment production. We reach the following specific conclusions:

1. Structure, topography, and sediment volume of the rifts are primarily controlled by the degree of strain localization
2. Rift systems with strong crust and a high degree of strain localization generate the highest sediment volumes. For a given erodibility, slower extending rifts produce more sediment than faster extending rifts, such that a reduction in extension rate by 50% increases the amount of sediment by 15%–40%
3. Feedback between erosion and deformation increases fault offset, enhancing rock uplift, and yielding more sediment. The effect is strongest for systems with efficient erosion (slow extension and high erodibility) and limited if the coupling between crust and mantle is low
4. We identify four characteristic phases for the morpho-tectonic and sediment flux evolution of rifts. Phase 1 early-stage rift initiation is associated with distributed faulting, low topography and erosion rates, which generates little sediment. Phase 2 is associated with uplift along the main rift bounding faults resulting in high erosion rates and a strong increase in sediment flux. Phase 3 basin-ward migration of fault activity is associated with slowly decreasing sediment flux. Post rift Phase 4 displays exponential decrease in sediment flux. Drainage capture of the hinterland during Phase 4 may lead to a transient increase in sediment flux. The phases of rifting reproduce many characteristics of natural rift systems and can be, for example, recognized in the northern North Sea, the Gulf of Suez, and the Gulf of Corinth
5. Our modeling results indicate that for natural examples, the approach of inverting the sedimentary record for the topographic evolution of rifts is promising. However, the peaks in rock uplift/maximum elevation predate the peak in sediment flux by 2–5 Myr (depending on the extension rate)

In summary, the evolution of a rift in terms of structures, topography and sediment flux reflects the complex interactions that can occur between tectonic and surface processes. We suggest that future work could include a more detailed analysis of geomorphic metrics (e.g., catchment area) or of the stratigraphic architecture. A comparison of these metrics from the model output with natural cases could also lead to a better understanding of the complicated processes behind continental rifting.

Data Availability Statement

As earth surface process model, we use the freely available, open source code FastScape (https://fastscape.org/), as outlined in the methods section. As thermo-mechanical model, we use the code Fantom (Thieulot, 2011), using the equations and procedure as outlined in the methods section. These models are used in a coupled manner to create the model output, and the data used for the analyses of the paper are available as animations at https://doi.org/10.6084/m9.figshare.18039509.v1 (Wolf et al., 2022).

Acknowledgments
The work presented in this study was funded by Total Energies through the COLORS project. RLG acknowledges a VISTA professorship from the Norwegian Academy of Science and Letters. We acknowledge computational resources by Uninett Sigma2 for project NN4704K. The authors thank the editor Isabelle Manighetti and associate editor Fabio Capitano for editorial handling, and reviewers Sascha Brune and Patrice Rey for helpful comments that improved the manuscript. The authors thank Thomas Theunissen for fruitful discussions and his help for setting up the strain inheritance of the models. The authors also acknowledge discussions with Brendan Simon about the geology and sedimentary history of Lake Albert.

References

Adams, B. A., Hodges, K. V., Whipple, K. X., Ehlers, T. A., Soest, M. C., & Wartho, J. (2015). Constraints on the tectonic and landscape evolution of the Bhutan Himalaya from thermochronometry: Late Cenozoic evolution of Bhutan. *Tectonics*, *34*(6), 1329–1347. https://doi.org/10.1002/2015TC003853

Allen, P. A. (2008). Time scales of tectonic landscapes and their sediment routing systems. *Geological Society, London, Special Publications*, *296*(1), 7–28. https://doi.org/10.1144/SP296.2

Allen, P. A., & Heller, P. L. (2011). Dispersal and preservation of tectonically generated Alluvial Gravels in sedimentary basins. In *Tectonics of sedimentary basins* (pp. 111–130). John Wiley & Sons, Ltd. https://doi.org/10.1002/9781444347166.ch6

Andrés-Martínez, M., Pérez-Gussinyé, M., Armitage, J., & Morgan, J. P. (2019). Thermomechanical implications of sediment transport for the architecture and evolution of continental rifts and margins. *Tectonics*, *38*(2), 641–665. https://doi.org/10.1029/2018TC005346

Armitage, J. J., Duller, R. A., Whittaker, A. C., & Allen, P. A. (2011). Transformation of tectonic and climatic signals from source to sedimentary archive. *Nature Geoscience*, *4*(4), 231–235. https://doi.org/10.1038/ngeo1087

Beaumont, C., Fullsack, P., & Hamilton, J. (1992). Erosional control of active compressional orogens. In K. R. McClay (Ed.), *Thrust tectonics* (pp. 1–18). Springer Netherlands. https://doi.org/10.1007/978-94-011-3066-0_1

Beucher, R., & Huismans, R. S. (2020). Morphotectonic evolution of passive margins undergoing active surface processes: Large-scale experiments using numerical models. *Geochemistry, Geophysics, Geosystems*, *21*(5), e2019GC008884. https://doi.org/10.1029/2019gc008884

Bialas, R. W., & Buck, W. R. (2009). How sediment promotes narrow rifting: Application to the Gulf of California. *Tectonics*, *28*. https://doi.org/10.1029/2008tc002394

Braun, J., & Willett, S. D. (2013). A very efficient O(n), implicit and parallel method to solve the stream power equation governing fluvial incision and landscape evolution. *Geomorphology*, *180–181*, 170–179. https://doi.org/10.1016/j.geomorph.2012.10.008

Brewer, C. J., Hampson, G. J., Whittaker, A. C., Roberts, G. G., & Watkins, S. E. (2020). Comparison of methods to estimate sediment flux in ancient sediment routing systems. *Earth-Science Reviews*, *207*, 103217. https://doi.org/10.1016/j.earscirev.2020.103217

Brune, S., Heine, C., Perez-Gussinye, M., & Sobolev, S. V. (2014). Rift migration explains continental margin asymmetry and crustal hyper-extension. *Nature Communications*, *5*.

Buiter, S. J. H., Huismans, R. S., & Beaumont, C. (2008). Dissipation analysis as a guide to mode selection during crustal extension and implications for the styles of sedimentary basins. *Journal of Geophysical Research: Solid Earth*, *113*(B6). https://doi.org/10.1029/2007JB005272

Castelltort, S., & Van Den Driessche, J. (2003). How plausible are high-frequency sediment supply-driven cycles in the stratigraphic record? *Sedimentary Geology*, *157*(1–2), 3–13. https://doi.org/10.1016/S0037-0738(03)00066-6

Champagnac, J.-D., Molnar, P., Sue, C., & Herman, F. (2012). Tectonics, climate, and mountain topography. *Journal of Geophysical Research: Solid Earth*, *117*(B2). https://doi.org/10.1029/2011JB008348

Corti, G., Molin, P., Sembroni, A., Bastow, I. D., & Keir, D. (2018). Control of pre-rift lithospheric structure on the architecture and evolution of continental rifts: Insights from the main Ethiopian rift, East Africa. *Tectonics*, *37*(2), 477–496. https://doi.org/10.1002/2017TC004799

Cowie, P., Underhill, J., Behn, M., Lin, J., & Gill, C. (2005). Spatio-temporal evolution of strain accumulation derived from multi-scale observations of late Jurassic rifting in the northern North sea: A critical test of models for lithospheric extension. *Earth and Planetary Science Letters*, *234*(3–4), 401–419. https://doi.org/10.1016/j.epsl.2005.01.039

Culling, W. E. H. (1963). Soil creep and the development of hillside slopes. *The Journal of Geology*, *71*(2), 127–161. https://doi.org/10.1086/626891

Densmore, A. L., Allen, P. A., & Simpson, G. (2007). Development and response of a coupled catchment fan system under changing tectonic and climatic forcing. *Journal of Geophysical Research*, *112*(F1). https://doi.org/10.1029/2006JF000474

Enkelmann, E., Zeitler, P. K., Pavlis, T. L., Garver, J. I., & Ridgway, K. D. (2009). Intense localized rock uplift and erosion in the St Elias orogen of Alaska. *Nature Geoscience*, *2*(5), 360–363. https://doi.org/10.1038/ngeo502

Erdős, Z., Huismans, R. S., & Beek, P. (2015). First-order control of syntectonic sedimentation on crustal-scale structure of mountain belts. *Journal of Geophysical Research: Solid Earth*, *120*(7), 5362–5377. https://doi.org/10.1002/2014JB011785

Fazlikhani, H., Aagotnes, S. S., Refvem, M. A., Hamilton-Wright, J., Bell, R. E., Fossen, H., et al. (2021). Strain migration during multiphase extension, Stord Basin, northern North Sea rift. *Basin Research*, *33*(2), 1474–1496. https://doi.org/10.1111/bre.12522

Ford, M., Hemelsdaël, R., Mancini, M., & Palyvos, N. (2017). Rift migration and lateral propagation: Evolution of normal faults and sediment-routing systems of the western Corinth rift (Greece). *Geological Society, London, Special Publications*, *439*(1), 131–168. https://doi.org/10.1144/SP439.15

Forzoni, A., Storms, J. E. A., Whittaker, A. C., & Jager, G. (2014). Delayed delivery from the sediment factory: Modeling the impact of catchment response time to tectonics on sediment flux and fluvio-deltaic stratigraphy. *Earth Surface Processes and Landforms*, *39*(5), 689–704. https://doi.org/10.1002/esp.3538

Fossen, H., Ksienzyk, A. K., Rotevatn, A., Bauck, M. S., & Wemmer, K. (2021). From widespread faulting to localised rifting: Evidence from K-Ar fault gouge dates from the Norwegian North Sea rift shoulder. *Basin Research*, *33*(3), 1934–1953. https://doi.org/10.1111/bre.12541

Gawthorpe, R. L., Jackson, C. A.-L., Young, M. J., Sharp, I. R., Moustafa, A. R., & Leppard, C. W. (2003). Normal fault growth, displacement localisation and the evolution of normal fault populations: The Hammam Faraun fault block, Suez rift, Egypt. *Journal of Structural Geology*, *25*(6), 883–895. https://doi.org/10.1016/S0191-8141(02)00088-3

Gawthorpe, R. L., Leeder, M. R., Kranis, H., Skourtsos, E., Andrews, J. E., Henstra, G. A., et al. (2018). Tectono-sedimentary evolution of the Plio-Pleistocene Corinth rift, Greece. *Basin Research*, *30*(3), 448–479. https://doi.org/10.1111/bre.12260

Geurts, A. H., Whittaker, A. C., Gawthorpe, R. L., & Cowie, P. A. (2020). Transient landscape and stratigraphic responses to drainage integration in the actively extending central Italian Apennines. *Geomorphology*, *353*, 107013. https://doi.org/10.1016/j.geomorph.2019.107013

Gleason, G. C., & Tullis, J. (1995). A flow law for dislocation creep of quartz aggregates determined with the molten salt cell. *Tectonophysics*, *247*(1), 1–23. https://doi.org/10.1016/0040-1951(95)00011-B

Grujic, D., Coutand, I., Bookhagen, B., Bonnet, S., Blythe, A., & Duncan, C. (2006). Climatic forcing of erosion, landscape, and tectonics in the Bhutan Himalayas. *Geology*, *34*(10), 801–804. https://doi.org/10.1130/G22648.1

Guillocheau, F., Rouby, D., Robin, C., Helm, C., Rolland, N., Le Carlier de Veslud, C., & Braun, J. (2012). Quantification and causes of the terrigenous sediment budget at the scale of a continental margin: A new method applied to the Namibia-South Africa margin. *Basin Research*, *24*(1), 3–30. https://doi.org/10.1111/j.1365-2117.2011.00511.x

Hemelsdaël, R., Ford, M., Malartre, F., & Gawthorpe, R. (2017). Interaction of an antecedent fluvial system with early normal fault growth: Implications for syn-rift stratigraphy, western Corinth rift (Greece). *Sedimentology*, *64*(7), 1957–1997. https://doi.org/10.1111/sed.12381

Huismans, R. S., & Beaumont, C. (2002). Asymmetric lithospheric extension: The role of frictional plastic strain softening inferred from numerical experiments *Geology* (Vol. *30*, pp. 2112–2214). https://doi.org/10.1130/0091-7613(2002)030<0211:aletro>2.0.co;2

Huismans, R. S., & Beaumont, C. (2003). Symmetric and asymmetric lithospheric extension: Relative effects of frictional-plastic and viscous strain softening. *Journal of Geophysical Research: Solid Earth*, *108*(B10). https://doi.org/10.1029/2002JB002026

Huismans, R. S., & Beaumont, C. (2011). Depth-dependent extension, two-stage breakup and cratonic underplating at rifted margins. *Nature*, *473*(7345), 74–78. https://doi.org/10.1038/nature09988

Karato, S., & Wu, P. (1993). Rheology of the upper mantle: A synthesis. *Science*, *260*(5109), 771–778. https://doi.org/10.1126/science.260.5109.771

Korchinski, M., Teyssier, C., Rey, P. F., Whitney, D. L., & Mondy, L. (2021). Single-phase vs two-phase rifting: Numerical perspectives on the accommodation of extension during continental break-up. *Marine and Petroleum Geology*, *123*, 104715. https://doi.org/10.1016/j.marpetgeo.2020.104715

Li, Q., Gasparini, N. M., & Straub, K. M. (2018). Some signals are not the same as they appear: How do erosional landscapes transform tectonic history into sediment flux records? *Geology*, *46*(5), 407–410. https://doi.org/10.1130/G40026.1

Mackwell, S. J., Zimmerman, M. E., & Kohlstedt, D. L. (1998). High-temperature deformation of dry diabase with application to tectonics on Venus. *Journal of Geophysical Research: Solid Earth*, *103*(B1), 975–984. https://doi.org/10.1029/97JB02671

Maniatis, G., Kurfeß, D., Hampel, A., & Heidbach, O. (2009). Slip acceleration on normal faults due to erosion and sedimentation — results from a new three-dimensional numerical model coupling tectonics and landscape evolution. *Earth and Planetary Science Letters*, *284*(3–4), 570–582. https://doi.org/10.1016/j.epsl.2009.05.024

McNeill, L. C., Shillington, D. J., Carter, G. D. O., Everest, J. D., Gawthorpe, R. L., Miller, C., et al. (2019). High-resolution record reveals climate-driven environmental and sedimentary changes in an active rift. *Scientific Reports*, *9*(1), 3116. https://doi.org/10.1038/s41598-019-40022-w

Michel, L., Ehlers, T. A., Glotzbach, C., Adams, B. A., & Stübner, K. (2018). Tectonic and glacial contributions to focused exhumation in the Olympic Mountains, Washington, USA. *Geology*, *46*(6), 491–494. https://doi.org/10.1130/G39881.1

Molnar, P., & England, P. (1990). Late Cenozoic uplift of mountain ranges and global climate change: Chicken or egg? *Nature*, *346*(6279), 29–34. https://doi.org/10.1038/346029a0

Naliboff, J. B., Buiter, S. J. H., Péron-Pinvidic, G., Osmundsen, P. T., & Tetreault, J. (2017). Complex fault interaction controls continental rifting. *Nature Communications*, *8*(1), 1179. https://doi.org/10.1038/s41467-017-00904-x

Olive, J.-A., Behn, M. D., & Malatesta, L. C. (2014). Modes of extensional faulting controlled by surface processes: Normal faulting and surface processes. *Geophysical Research Letters*, *41*(19), 6725–6733. https://doi.org/10.1002/2014GL061507

Rohais, S., Barrois, A., Colletta, B., & Moretti, I. (2016). Pre-salt to salt stratigraphic architecture in A rift basin: Insights from a basin-scale study of the Gulf of Suez (Egypt). *Arabian Journal of Geosciences*, *9*(4), 317. https://doi.org/10.1007/s12517-016-2327-8

Rohais, S., & Rouby, D. (2020). Source-to-Sink analysis of the Plio-Pleistocene deposits in the Suez rift (Egypt). In S. Khomsi, F. M. Roure, M. Al Garni, & A. Amin (Eds.), *Arabian plate and surroundings: Geology, sedimentary basins and georesources* (pp. 115–133). Springer International Publishing. https://doi.org/10.1007/978-3-030-21874-4_4

Simon, B. (2015). *Rift du Lac Albert, Ouganda, rift Est Africain: Déformation, érosion, sédimentation et bilan de matière depuis 17 Ma*. Retrieved from http://www.theses.fr/2015REN1S175/document

Sømme, T. O., Skogseid, J., Embry, P., & Løseth, H. (2019). Manifestation of tectonic and climatic perturbations in deep-time stratigraphy – an example from the Paleocene succession offshore western Norway. *Frontiers of Earth Science*, *7*, 303. https://doi.org/10.3389/feart.2019.00303

Stevens Goddard, A., Carrapa, B., & Aciar, R. H. (2020). Recognizing drainage reorganization in the stratigraphic record of the Neogene foreland basin of the Central Andes. *Sedimentary Geology*, *405*, 105704. https://doi.org/10.1016/j.sedgeo.2020.105704

Stock, J. D., & Montgomery, D. R. (1999). Geologic constraints on bedrock river incision using the stream power law. *Journal of Geophysical Research: Solid Earth*, *104*(B3), 4983–4993. https://doi.org/10.1029/98JB02139

Svartman Dias, A. E., Lavier, L. L., & Hayman, N. W. (2015). Conjugate rifted margins width and asymmetry: The interplay between lithospheric strength and thermomechanical processes. *Journal of Geophysical Research: Solid Earth*, *120*(12), 8672–8700. https://doi.org/10.1002/2015JB012074

Syvitski, J. P. M., & Milliman, J. D. (2007). Geology, geography, and humans battle for dominance over the delivery of fluvial sediment to the coastal ocean. *The Journal of Geology*, *115*(1), 1–19. https://doi.org/10.1086/509246

Tetreault, J. L., & Buiter, S. J. H. (2018). The influence of extension rate and crustal rheology on the evolution of passive margins from rifting to break-up. *Tectonophysics*, *746*, 155–172. https://doi.org/10.1016/j.tecto.2017.08.029

Theunissen, T., & Huismans, R. S. (2019). Long-term coupling and feedback between tectonics and surface processes during non-Volcanic rifted margin formation. *Journal of Geophysical Research: Solid Earth*, *124*(11), 12323–12347. https://doi.org/10.1029/2018JB017235

Thieulot, C. (2011). Fantom: Two- and three-dimensional numerical modelling of creeping flows for the solution of geological problems. *Physics of the Earth and Planetary Interiors*, *188*(1–2), 47–68. https://doi.org/10.1016/j.pepi.2011.06.011

Walford, H., White, N., & Sydow, J. (2005). Solid sediment load history of the Zambezi Delta. *Earth and Planetary Science Letters*, *238*(1–2), 49–63. https://doi.org/10.1016/j.epsl.2005.07.014

Wang, P., Scherler, D., Liu-Zeng, J., Mey, J., Avouac, J.-P., Zhang, Y., & Shi, D. (2014). Tectonic control of Yarlung Tsangpo Gorge revealed by a buried canyon in Southern Tibet. *Science*, *346*(6212), 978–981. https://doi.org/10.1126/science.1259041

Whipple, K. X. (2009). The influence of climate on the tectonic evolution of mountain belts. *Nature Geoscience*, *2*(2), 97–104. https://doi.org/10.1038/ngeo413

Whipple, K. X., & Tucker, G. E. (1999). Dynamics of the stream-power river incision model: Implications for height limits of mountain ranges, landscape response timescales, and research needs. *Journal of Geophysical Research: Solid Earth*, *104*(B8), 17661–17674. https://doi.org/10.1029/1999JB900120

Whittaker, A. C. (2012). How do landscapes record tectonics and climate? *Lithosphere*, *4*(2), 160–164. https://doi.org/10.1130/RF.L003.1

Whittaker, A. C., Attal, M., & Allen, P. A. (2010). Characterising the origin, nature and fate of sediment exported from catchments perturbed by active tectonics. *Basin Research*, *22*(6), 809–828. https://doi.org/10.1111/j.1365-2117.2009.00447.x

Willett, S. D. (1999). Orogeny and orography: The effects of erosion on the structure of mountain belts. *Journal of Geophysical Research: Solid Earth*, *104*(B12), 28957–28981. https://doi.org/10.1029/1999jb900248

Wolf, L., Huismans, R. S., Rouby, D., Gawthorpe, R. L., & Wolf, S. (2022). Data and animations for manuscript by Wolf et al. (2022) entitled: "Links between faulting, topography, and sediment production during continental rifting: Insights from coupled surface process, thermo-mechanical modelling. *figshare*. https://doi.org/10.6084/m9.figshare.18039509.v1

Wolf, S. G., Huismans, R. S., Muñoz, J., Curry, M. E., & Beek, P. (2021). Growth of collisional orogens from small and cold to large and hot—inferences from geodynamic models. *Journal of Geophysical Research: Solid Earth*, *126*(2). https://doi.org/10.1029/2020JB021168

Yuan, X. P., Braun, J., Guerit, L., Rouby, D., & Cordonnier, G. (2019). A new efficient method to solve the stream power law model taking into account sediment deposition. *Journal of Geophysical Research: Earth Surface*, *124*(6), 1346–1365. https://doi.org/10.1029/2018jf004867